



Chromium evidence for protracted oxygenation during the Paleoproterozoic



Kaarel Mänd^{a,b,*}, Noah J. Planavsky^c, Susannah M. Porter^d, Leslie J. Robbins^e,
Changle Wang^{f,g,h}, Timmu Kreitsmann^{b,i}, Kärt Paiste^{b,j}, Päärn Paiste^b,
Alexander E. Romashkin^{k,1}, Yulia E. Deines^k, Kalle Kirsimäe^b, Aivo Lepland^{b,l,m},
Kurt O. Konhauser^a

^a Department of Earth & Atmospheric Sciences, University of Alberta, Edmonton, Alberta, Canada

^b Department of Geology, University of Tartu, Tartu, Estonia

^c Department of Earth and Planetary Sciences, Yale University, New Haven, CT, USA

^d Department of Earth Science, University of California at Santa Barbara, Santa Barbara, CA 93106, USA

^e Department of Geology, University of Regina, Regina, Saskatchewan, Canada

^f Key Laboratory of Mineral Resources, Institute of Geology and Geophysics, Chinese Academy of Sciences, Beijing 100029, China

^g Institutions of Earth Science, Chinese Academy of Sciences, Beijing 100029, China

^h University of Chinese Academy of Sciences, Beijing 100049, China

ⁱ Department of Physics and Earth Sciences, Jacobs University Bremen, 28759 Bremen, Germany

^j Department of Earth and Planetary Sciences, Washington University in St. Louis, St. Louis, MO 63130, USA

^k Institute of Geology, Karelian Research Centre, Russian Academy of Sciences, Petrozavodsk, Russia

^l CAGE—Centre for Arctic Gas Hydrate, Environment and Climate, Department of Geosciences, UiT The Arctic University of Norway, Tromsø, Norway

^m Geological Survey of Norway (NGU), Trondheim, Norway

ARTICLE INFO

Article history:

Received 2 August 2021

Received in revised form 7 March 2022

Accepted 10 March 2022

Available online xxx

Editor: B. Wing

Keywords:

Cr isotopes

oxygen overshoot

isotope geochemistry

eukaryotes

ABSTRACT

It has commonly been proposed that the development of complex life is tied to increases in atmospheric oxygenation. However, there is a conspicuous gap in time between the oxygenation of the atmosphere 2.4 billion years ago (Ga) and the first widely-accepted fossil evidence for complex eukaryotic cells < 1.7 Ga. At present the gap could either represent poor sampling, poor preservation, and/or difficulties in recognizing early eukaryote fossils, or it could be real and the evolution of complex cells was delayed due to relatively low and/or variable O₂ levels in the Paleoproterozoic. To assess the extent and stability of Paleoproterozoic O₂ levels, we measured chromium-based oxygen proxies in a > 2400-m core from the Omega Basin (NW-Russia), deposited ~ 2.1–2.0 billion years ago—a few hundred million years prior to the oldest definitive fossil evidence for eukaryotes. Fractionated chromium isotopes are documented throughout the section (max. 1.63 ± 0.10‰ δ⁵³Cr), suggesting a long interval (possibly > 100 million years) during which oxygen levels were higher and more stable than in the billion years before or after. This suggests that, if it is the case that complex cells did not evolve until after 1.7 Ga, then this delay was not due to O₂-limitation. Instead, it could reflect other limiting factors—ecological or environmental—or could indicate that it simply takes a long time—more than the tens to >100 million years recorded in Omega Basin sediments—for such biological innovations to evolve.

© 2022 Elsevier B.V. All rights reserved.

1. Introduction

Free O₂ in the atmosphere, the result of oxygenic photosynthesis, shapes ecology on the global scale. Understanding Earth's

oxygenation is therefore paramount to understanding the evolution and history of life. Given that O₂-dependent metabolisms are highly energetic and that atmospheric O₂ concentrations (pO₂) correlate with increased nutrient richness (Reinhard et al., 2020), high oxygen levels are often, though controversially, thought to be necessary for 'complex' (e.g., eukaryotic) life (Cole et al., 2020). A distinct, but related question is whether high pO₂ alone is sufficient for this purpose—or in other words, was oxygenation the trigger for shifts towards more complex life. In this view, removing the O₂-limitation will quickly lead to the evolution of traits

* Corresponding author at: University of Tartu, Department of Geology, Ravila 14a, Tartu 50411, Estonia.

E-mail address: kaarel.mand@ut.ee (K. Mänd).

¹ Deceased Feb. 16, 2021.

thought to underpin complexity, including eukaryote-grade cells, large size, and multicellularity (e.g., Payne et al., 2009; Zhang et al., 2018), implying that pO_2 above all else modulated the evolution of complex life on Earth (cf. Catling et al., 2005).

One challenge to this view is the mismatch between the appearance of unambiguous eukaryotic fossils in rocks younger than ~ 1.7 Ga (e.g., Agić et al., 2015, 2017; Adam et al., 2017; Javaux et al., 2001; Javaux and Knoll, 2017; Miao et al., 2019), and the initial oxygenation of the atmosphere 700 million years earlier (Farquhar et al., 2000; Warke et al., 2020). While this could be interpreted to suggest that O_2 levels were not the primary modulator of eukaryote emergence, others have hypothesized that O_2 levels simply were not stable or high enough to support substantial eukaryotic communities (Javaux and Lepot, 2018) before the latest Paleoproterozoic (Zhang et al., 2018).

A way to test this hypothesis is to examine the record of redox changes across an extended period of time in the early Proterozoic Eon prior to the first unambiguous eukaryotic fossils. The early Proterozoic witnessed the disappearance of mass-independent sulfur isotope fractionations by ~ 2.5 to 2.32 billion years ago (Ga) (Farquhar et al., 2000; Warke et al., 2020), signifying the permanent oxygenation of the atmosphere. This change is colloquially known as the Great Oxidation Event (GOE) (Holland, 2002). The Rhyacian Period (2.3–2.05 Ga) is notable for high positive carbon isotope fractionations in marine carbonates ($\delta^{13}C_{carb}$) (Karhu and Holland, 1996). As $\delta^{13}C_{carb}$ has been closely coupled to the burial of biomass and the release of O_2 accumulated in the atmosphere, this led Bekker and Holland (2012) to hypothesize that atmospheric O_2 levels may have reached 50% of the modern in this period. This is in accordance with signals of highly elevated seawater sulfate concentrations, including the deposition of massive evaporites (e.g., Blättler et al., 2018) and sedimentary sulfur isotope signatures (Planavsky et al., 2012), that point to a robust marine sulfate pool that is only stable in oxygenated conditions, but pO_2 remains difficult to robustly constrain.

A more recent approach has been to use the concentrations and isotopes of redox-sensitive trace metals to infer the amount of O_2 required to mobilize those elements from the crust to the oceans where they are subsequently incorporated into sedimentary rocks. However, this approach has led to conflicting results. For instance, Mänd et al. (2020) used the concentrations of molybdenum (Mo), rhenium (Re) and uranium (U), as well as U isotopes, in marine sediments to demonstrate that highly oxidized conditions continued up to around 2 Ga. Yet, the same Orosirian Period (2.05 to 1.8 Ga), and more generally the mid-Proterozoic (2 to 0.8 Ga), is generally thought to be characterized by lower levels of oxygen, as evidenced by muted sedimentary U concentrations (Partin et al., 2013), absent cerium (Ce) anomalies (Bellefroid et al., 2018), and reduced Mo isotope fractionations (Ossa Ossa et al., 2018, among others). In essence, different proxies present varying views of Earth's oxygenation due to their different spatial scales and sensitivities to pO_2 that, along with the fragmentary nature of studied sedimentary successions, hinder attempts to link oxygenation to preserved shifts in fossil complexity.

A continuous record of chromium isotope fractionations ($\delta^{53}Cr$) presents the opportunity for probing the stability of pO_2 in Earth's atmosphere, as substantial $\delta^{53}Cr$ fractionations are inherited from continental weathering environments in direct contact with atmospheric oxygen (Frei et al., 2009; Wei et al., 2020), although see Daye et al. (2019), Liu et al. (2020), and Lyons et al. (2020). Crucially, although $\delta^{53}Cr$ fractionations record mainly oxygen-poor weathering settings in the middle Proterozoic (Cole et al., 2016; Colwyn et al., 2019; Planavsky et al., 2014), with potential episodes of oxygenation (Canfield et al., 2018; Gilleaudeau et al., 2016; Wei et al., 2021), there is intriguingly no Cr isotope evidence for weathering under oxygen-rich environments in the middle

Paleoproterozoic—when it has been commonly proposed as a high-oxygen interval based on other proxies (Bekker and Holland, 2012; Blättler et al., 2018; Planavsky et al., 2012).

Amongst the best locations to establish a long, continuous Paleoproterozoic Cr record is the Onega Basin in the Karelian Republic, Russia (Melezhik et al., 2013). This is a > 3 -km-thick Paleoproterozoic succession of evaporites, carbonates, and siliciclastics, including organic-rich mudstones, intercalated with mafic igneous rocks (Fig. 1). In this study, we present new bulk-rock $\delta^{53}Cr$ data from a ~ 2400 -m-thick volcano-sedimentary drill core from the Onega Basin, obtained from the Onega Parametric Hole (OPH; drilled in 2008–2009 in the southern Onega Basin at 62.1559 N, 34.4073 E; Fig. 1). The drill core intersects ~ 800 m of the Tulomozero Formation, ~ 1500 m of the Zaonega Formation, and ~ 500 m of the Suisari Formation. We find that substantially fractionated sedimentary $\delta^{53}Cr$ values persist throughout the Onega Basin succession, across several facies transitions. This suggests that the Onega Basin records a protracted time period—possibly more than 100 million years (Myrs)—that was host to a fundamentally stable and oxygen-rich ocean-atmosphere system providing a platform to revisit the links between oxygen and the development of complex life.

2. The Onega Basin

The Onega Basin succession begins with the deposition of coarse-grained siliciclastics and lava flows onto a basement of Archean granites and gneisses. These are overlain by the ~ 800 -m-thick Tulomozero Formation (~ 2100 – 2050 Ma; see below for age references) made up of evaporites and dolomites. The Zaonega Formation (~ 2050 – 2000 Ma) follows as a ~ 1500 -m-thick volcano-sedimentary package consisting of dolostones, siliciclastic turbidites, and mudstones intercalated with mafic igneous rocks. On top of that lies the ~ 500 -m-thick Suisari Formation (~ 2000 – 1970 Ma) comprising mainly tuffs and mafic lavas/sills. The section is capped by fluvial-lacustrine siliciclastics of the Kondopoga Formation. Following deposition, the Onega Basin underwent greenschist-facies metamorphism during the ~ 1.89 – 1.79 Ga Svecofennian orogeny, which deformed the succession into a series of northwest–southeast trending folds (Melezhik et al., 2013, and references therein).

This study focuses on the Tulomozero, Zaonega, and Suisari formations that constitute the middle and upper part of the Onega Basin succession. There is significant lithofacies variation in the Tulomozero Formation—in the northern part of the basin, along with the western and eastern margins, the formation consists mainly of dolomite with varying amounts of magnesite and calcium sulphate pseudomorphs, and siliciclastic layers. By contrast, the formation in the southern part of the basin, as recorded by the drill core of the Onega Parametric Hole, begins with a ~ 600 -m-thick halite and anhydrite-magnesite unit that grades upwards into a dolomite dominated unit. It is likely that in its present northern extent the formation was deposited in a low-energy intertidal, sabkha or playa lake environment with fluvial influences, whereas the southern part of the basin was more restricted and evaporitic, but still experienced periodic seawater influx that sustained the accumulation of hundreds of meters of evaporites (Blättler et al., 2018; Melezhik et al., 2013). Carbonates of the Tulomozero Formation are characterized by strongly positive $\delta^{13}C_{carb}$ values, reaching as high as 18‰, that potentially reflect local amplification of a globally ^{13}C -enriched bicarbonate pool (e.g., Melezhik et al., 1999). As such, it is one of the type sections for the Lomagundi–Jatuli carbon isotope excursion (Karhu and Holland, 1996). The paragenesis of halite and calcium sulfate, together with their S and Ca isotope composition, have been taken as evidence of a large marine sulfate pool, constituting $> 30\%$ of modern levels (Blättler et al., 2018).

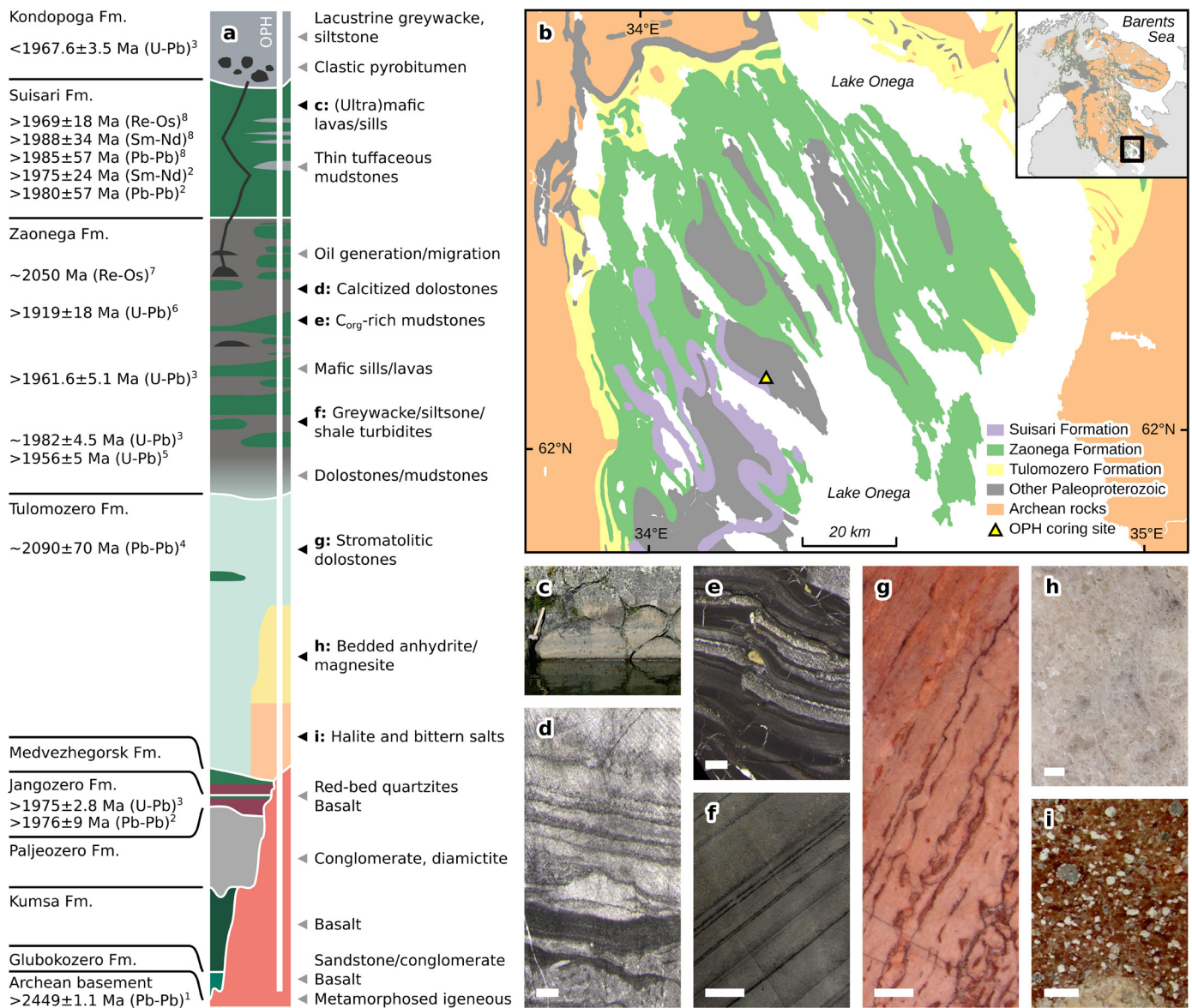


Fig. 1. Onega Basin geology. (a) Simplified stratigraphy of the Onega Basin sedimentary succession showing formation boundaries, age constraints (explained in text; superscripts are references: 1—Amelin et al., 1995; 2—Puchtel et al., 1998; 3—Martin et al., 2015; 4—Ovchinnikova et al., 2007; 5—Stepanova et al., 2014; 6—Priyatkina et al., 2014; 7—Bauer et al., 2019; 8—Puchtel et al., 1999), predominant geological features, and the location of the Onega Parametric Hole (OPH). Modified from Melezhik et al. (2015) and Paiste et al. (2018). (b) The exposures of the Tulomozero, Zaonega, and Suisari formations within the Onega Basin, NW Russia are shown by color. (c) Mafic pillow lavas of the Suisari Formation. Hammer head is ~15 cm across (outcrop on the western shore of Lake Onega, Melezhik et al., 2013). (d–i) Polished drill core photographs of common rock types of the Tulomozero and Zaonega formations. Scale bars are 1 cm across. (d) Laminated fine-grained dolostone in the upper Zaonega Formation (OnZaP drill cores, northern Onega Basin, 13 m, Paiste et al., 2018). (e) Laminated organic- and sulphide-rich mudstone in the upper Zaonega Formation displaying soft-sediment deformation as well as quartz-mica and pyrobitumen veining (OnZaP, 63 m, Paiste et al., 2018). (f) Rhythmically bedded greywacke-siltstone in the lower Zaonega Formation (FAR-DEEP 12AB drill core, northern Onega Basin, 282 m, Melezhik et al., 2013). (g) Pale pink dolostone of the upper Tulomozero formation with red-brown stromatolitic laminae (FAR-DEEP 11A drill core, northern Onega Basin, 107 m, Melezhik et al., 2013). (h) Massive, coarse-crystalline anhydrite in the middle Tulomozero Formation (OPH, 2510 m, Melezhik et al., 2015). (i) Brown and pink, massive, coarse-grained halite of the lower Tulomozero Formation with inclusions of anhydrite (white), magnesite (yellow), and shale (pale gray) (OPH, 2902 m, Melezhik et al., 2015). (For interpretation of the colors in the figure(s), the reader is referred to the web version of this article.)

The overlying Zaonega Formation was, in contrast, deposited in alternating shallow and deeper water conditions, possibly in a rift basin developed on a highly active continental margin. Between 35–70% of the succession is composed of mafic sills and lavas emplaced into unconsolidated sediments (Melezhik et al., 2013). The lowermost Zaonega Formation is dominated by mudstones with common dolostone interbeds which transition into deeper-water mixed mudstones, dolostones, and siliciclastic rhythmites further up section. The formation is notable for containing extremely high organic carbon content (up to 70 wt.%), the earliest known oil field (Qu et al., 2012), highly elevated redox-sensitive element concentrations (Mänd et al., 2020), and one of the earliest sedimentary

phosphorus enrichments (Lepland et al., 2014). Variable and often high pyrite S isotope ratios have been interpreted as recording a diminished global marine sulfate pool or, alternatively, anomalously high local sulfate demand by microorganisms (Paiste et al., 2020b, and references therein). In the lower part of the Zaonega Formation, dolostones enriched in ¹³C record the Lomagundi–Jatuli excursion (Melezhik et al., 2015), but the best-preserved carbonates of the upper Zaonega Formation have normal-marine ^δ¹³C values (Kreitsmann et al., 2020, 2019). Strongly negative ^δ¹³C values in carbonates and organic matter from the middle part of the Zaonega Formation were earlier thought to reflect a global negative C isotope excursion but are now viewed as artifacts of hydrothermal

de-dolomitization (Kreitsmann et al., 2020, and references therein) and the incorporation of methanotrophic biomass (Qu et al., 2012).

The deposition of the Zaonega Formation was followed by the Suisari Formation. The latter signifies a slowdown of subsidence and the infilling of the basin with hundreds-of-meters-thick subaqueous mafic-to-ultramafic lavas and sills interlayered with relatively thin, tuffaceous mudstone beds (Melezhik et al., 2013).

The age of the Onega Basin remains imprecisely constrained (Fig. 1a). The most robust anchor for the older age boundary is given by a Pb–Pb age of 2449 ± 1.1 million years ago (Ma) from a pluton crosscutting the Archean basement (Amelin et al., 1995). The Tulomozero Formation is additionally constrained by an imprecise dolomite Pb–Pb age of 2090 ± 70 Ma (Ovchinnikova et al., 2007) and by virtue of it recording the Lomagundi–Jatuli isotope excursion (along with the lowermost Zaonega Formation), which terminated in Fennoscandia at ~ 2060 Ma (Martin et al., 2013). A single zircon from a tuff layer in the lower Zaonega Formation yielded a U–Pb age of 1982 ± 4.5 Ma (Martin et al., 2015). A suite of cross-cutting dykes and sills in the Onega Basin succession provide younger age boundaries. A mafic sill in the Jangozero Formation, below the Tulomozero Formation, has yielded U–Pb zircon and baddeleyite ages of 1976 ± 9 Ma (Puchtel et al., 1998) and 1975.3 ± 2.8 (Martin et al., 2015). Zircons in dolerite and kimberlite sills in the Zaonega Formation have been U–Pb dated to 1919 ± 18 Ma (Priyatkina et al., 2014), 1956 ± 5 Ma (Stepanova et al., 2014), and 1961 ± 5.1 Ma (Martin et al., 2015); some of these sills have peperitic contacts, implying that the sediments were still wet and unconsolidated at the time of intrusion. Gabbro sills of the Suisari Formation, interpreted as coeval to the platform lavas, are dated 1975 ± 24 (whole-rock and clinopyroxene Sm–Nd), 1980 ± 57 Ma (leach residue, plagioclase, and clinopyroxene Pb–Pb, Puchtel et al., 1998), 1988 ± 34 Ma (whole-rock and clinopyroxene Sm–Nd), 1985 ± 57 Ma (whole-rock and plagioclase Pb–Pb), and 1969 ± 18 Ma (whole-rock, ilmenite, and ulvöspinel Re–Os, Puchtel et al., 1999). Re–Os dates on Zaonega Formation mudstones have yielded a preliminary, and not yet peer-reviewed, age of ~ 2050 Ma (Bauer et al., 2019). Finally, a sandstone in the overlying Kondopoga Formation yielded a detrital zircon Pb–Pb age of 1967 ± 3.5 Ma (Martin et al., 2015). In summary, while dates are imprecise, deposition of the ~ 2400 -m-thick succession comprising the Tulomozero, Zaonega, and Suisari formations likely spanned several tens of millions and possibly over a hundred million years. Provisionally, we constrain the age of the succession between ~ 2.1 – 2.0 Ga.

3. Materials and methods

3.1. Drill core

Drill core samples were obtained from the ~ 3500 -m-long Onega Parametric Hole (OPH), drilled in 2008–2009 in the southern Onega Basin (62.1559 N, 34.4073 E; Fig. 1). The drill core intersects ~ 800 m of the Tulomozero Formation, ~ 1500 m of the Zaonega Formation, and ~ 500 m of the Suisari Formation. Samples for this study were obtained from each of the aforementioned formations and constitute three sample sets: “NGU” (140 samples), “ACME” (40 samples), and “Yale” (73 samples). Care was taken to remove any macroscopically visible veins or monocrystalline mineral grains from rock slabs, especially for the “Yale” samples from which Cr isotope compositions were measured.

3.2. X-ray diffraction

The mineralogical composition of 147 samples was studied using X-ray diffractometry (XRD) at the University of Tartu, Estonia.

Rock samples were ground to a fine powder, pressed into un-oriented tablets and scanned on a Bruker D8 Advance diffractometer, where a copper $K\alpha$ X-ray source and a LynxEye positive sensitive detector were used to generate diffractograms in a 2 – 70° 2θ range. Quantitative mineral abundances were modeled using the Rietveld algorithm-based Topaz software suite. The relative error for major mineral components (> 5 wt.%) was $\sim 10\%$ and $\sim 20\%$ for minor mineral components (< 5 wt.%).

Based on the results, the samples were divided into three main lithotypes: (1) evaporites (containing > 10 wt.% halite, magnesite, and/or anhydrite) which mainly occur below 2330 m depth; (2) carbonates (containing > 50 wt.% dolomite, calcite, magnesite, and/or siderite) above 2330 m depth that are dominated by dolomite and magnesite in the Tulomozero Formation, and dolomite–calcite in the Zaonega Formation; and (3) mudstones which first appear above 2330 m, but become dominant in the Zaonega Formation, where they contain mostly quartz, feldspars, micas and chlorite. See Supplementary Text for a more detailed description. For some mudstone and carbonate samples, mineralogical data was not available. For classification, the carbonate content of these samples was, instead, estimated using elemental abundances and the formula $(Ca + Mg)/(Si + Al)$, with values > 0.5 being considered carbonates.

3.3. Element abundances

Total organic carbon (TOC) content was measured at the Geological Survey of Norway (NGU) using a LECO SC-444 analyser (“NGU” samples) (Paiste et al., 2020a) and at the University of Alberta via loss on ignition (“ACME” and “Yale” samples). For the latter, sample aliquots weighing between 0.5 and 2 g were loaded into ceramic beakers and combusted at 500°C for 8–12 h, and the change in mass was recorded. Element concentrations for sample set “NGU” were determined at NGU with a Philips PW 1480 X-ray fluorescence spectrometer equipped with a rhodium X-ray tube. For major elements, 0.6 g of powdered sample aliquots and 4.2 g of $\text{Li}_2\text{B}_4\text{O}_7$ were heated to 1000°C and fused into a bead using a CLAISSE FLUXER-BIS. For minor elements, samples were prepared by mixing 9.6 g of powdered sample with 2.4 g of Hoechst wax in a Spex Mixer/Mill and pressing them into a pellet using a Herzog press. The detection limits for major elements were generally below 0.02% and the typical precision (1σ) was $\sim 2\%$. For minor elements, detection limits were $\leq 10 \mu\text{g g}^{-1}$. Calibration of the XRF was done using a set of ~ 120 internationally certified natural rock standards as well as ~ 20 artificial standards provided by the XRF manufacturer.

Element concentrations for sample set “ACME” were determined at ACME Laboratories, Bureau Veritas Commodities Canada Ltd. The samples were powdered and then heated to mineralize organic carbon. Major elements were analyzed via inductively coupled plasma optical emission spectroscopy (ICP-OES) from aliquots fused into a LiBO_2 bead. Minor elements were digested using a mix of HNO_3 , HClO_4 , and HF and analyzed via inductively coupled plasma mass spectrometry (ICP-MS). Average relative standard deviation was less than 5% for all elements; accuracy was monitored using the OREAS 25a and OREAS 45e reference materials.

Element concentrations of sample set “Yale” were measured at the Yale Metal Geochemistry Center (YMGC). The samples were pulverized in an agate mill, combusted in ceramic crucibles at 500°C for 8 h to remove organic carbon and digested in a class ten Pico-trace clean laboratory using a succession of concentrated, Teflon-distilled acids. Digestions were initiated with the addition of 3 ml of HNO_3 and 1 ml of HF , then heated at 100°C for 24 h in closed Teflon vials, before being evaporated to dryness. Once dry, 3 ml HCl and 1 ml of HNO_3 were added to each sample, and samples were heated at 95°C for 24 h before being dried down.

Final residues were then taken up in 5 mL of 3N HNO₃ solution at 70°C for 1 h. Prior to analyses by ICP-MS, samples were diluted 200:1 in 5% Teflon-distilled HNO₃ spiked with 1 ng g⁻¹ indium (In). All samples were measured on a Thermo Scientific Element XR high-resolution ICP-MS. The In spike was used to correct for instrumental drift over the analytical session. Five dilutions of a customized internal laboratory standard were measured at the end and beginning of the analyses and several times throughout the run. Repeat analysis on the laboratory standard yielded a relative standard deviation (1σ) for all elements (excepting Na) of ≤ 8%, averaging ~ 4% across the analytical session. External accuracy was assessed by measuring the geostandard BHVO-2; relative difference between measured and known values for all elements was 8.3% on average and generally below 10%. In particular, the Cr and Ti values for BHVO-2 were within the 95% confidence interval for accepted values (Jochum et al., 2005). For all sample sets, Cr was normalized to the detrital tracer element Ti to assess authigenic enrichments, as suggested by Cole et al. (2017).

3.4. Isotope ratios

Oxygen isotope ratios of carbonates from micro-drilled samples were measured at the University of Tartu using a Thermo Scientific Delta V Advantage continuous flow isotope ratio mass spectrometer and include data published in Kreitsmann et al. (2019). The precision of the measurements was 0.2‰ (2σ) and the long-term reproducibility exceeded ±0.2‰ (2σ). The compositions are expressed as the ratio of ¹⁸O over ¹⁶O, normalized to the Vienna Pee Dee Belemnite (VPDB) reference standard as δ¹⁸O:

$$\delta^{18}\text{O} = \left[\left(\frac{{}^{18}\text{O}/{}^{16}\text{O}}{\text{sample}} \right) / \left(\frac{{}^{18}\text{O}/{}^{16}\text{O}}{\text{VPDB}} \right) - 1 \right] \times 1000\text{‰} \quad (1)$$

A correction was applied for the differing phosphoric acid fractionation factor of dolomite and calcite (Rosenbaum and Sheppard, 1986) according to the mineralogy of individual samples. Oxygen isotope compositions of bulk samples are presented here as an average of several micro-drilled sub-samples (1–7 micro-drilled measurements per bulk sample).

Chromium isotope compositions were determined for the “Yale” sample set at the YMGC from solutions prepared for elemental concentration analysis (see above). Sample preparation adapted the methods of Schoenberg et al. (2008) and Reinhard et al. (2014). An aliquot of each sample, containing ~ 200 ng of Cr, was diluted in 2 ml of 6N HCl and a ⁵⁰Cr–⁵⁴Cr double spike was added at a spike/sample ratio of ~ 0.5, in order to correct for isotope fractionation during sample processing and measurement (Schoenberg et al., 2008). The samples were purified chromatographically to remove mass interference from ⁵⁴Fe, ⁵⁰Ti, and ⁵⁰V (see Supplementary Information). First, samples were passed through columns containing AG1-X8 anionic resin, where the matrix was eluted by addition of 0.2N HCl and Cr was subsequently collected with 2N HNO₃. Second, samples were loaded on microcolumns filled with AG1-X8 resin to remove all remaining Fe, and Cr was eluted with 6N HCl. In the final step, Ti was removed using the cationic resin AG50W-X8: the matrix was eluted with 0.5N HNO₃, 0.5N HF, and 1N HCl and Cr was subsequently released with 1.8N HCl. Residues were taken up in 5% HNO₃ and analyzed on a Thermo-Finnigan Neptune Plus multicollector ICP-MS. To correct for remaining interferences, the samples were run in high-resolution mode and Fe, Ti, and V were monitored. Standard-sample bracketing with the NIST SRM 979 reference standard was employed to correct for instrumental drift. Instrumental mass bias and fractionation during sample preparation was corrected for using the Cr double-spike. Chromium isotopic compositions are normalized to the composition of the reference material NIST SRM 979, and reported as:

$$\delta^{53}\text{Cr} = \left[\left(\frac{{}^{53}\text{Cr}/{}^{52}\text{Cr}}{\text{sample}} \right) / \left(\frac{{}^{53}\text{Cr}/{}^{52}\text{Cr}}{\text{SRM979}} \right) - 1 \right] \times 1000\text{‰} \quad (2)$$

The internal precision was calculated based on 20 duplicate analyses of NIST SRM 979 and reported as 2σ uncertainty. Geostandards BHVO-2B and Nod-1-a were used to monitor the external precision; the measured values were between –0.13‰ to –0.10‰ and 0.04‰ to 0.09‰, respectively, which are within error of previously reported measurements (Cole et al., 2016).

3.5. In-situ element mapping

In-situ element mapping of two polished samples (OPH-1572 and OPH-4081) from representative lithologies was conducted at the University of Tartu. Mapping involved parallel laser scans perpendicular to bedding from areas containing secondary silicate veins and anhydrite. Scans were performed with a Cetac LSX-213 G2+ laser system with a HelEx II fast-washout two-volume large-format cell using 800 ml min⁻¹ helium as carrier gas. A square 65 μm laser spot moving left-to-right at 65 μm s⁻¹ at 10 Hz and a power of 3.45 J cm⁻² was used. The total duty cycle was 0.2 s. For sample OPH-4081, ²⁴Mg, ²⁷Al, ²⁸Si, ³¹P, ³⁴S, ³⁹K, ⁴³Ca, ⁴⁹Ti, ⁵¹V, ⁵²Cr, ⁵⁵Mn, ⁵⁶Fe, ⁶⁰Ni, ⁶³Cu, ⁶⁶Zn, ⁸⁸Sr, ⁸⁹Y, ¹³⁷Ba, ¹⁴⁰Ce, and ²³⁸U were measured at a dwell time of 7 ms. For sample OPH-1572, ¹³C, ²⁷Al, ²⁸Si, ³¹P, ³⁴S, ⁴³Ca, ⁴⁷Ti, ⁵¹V, ⁵²Cr, ⁵⁵Mn, ⁵⁶Fe, ⁶⁰Ni, ⁶³Cu, ⁶⁶Zn, ⁹⁵Mo, ¹⁴⁰Ce, and ²³⁸U were measured at a dwell time of 8 ms. The composition of the volatilized material was analyzed using an Agilent 8800 quadrupole ICP-MS in single quad mode. Maps are presented as relative abundances in counts per second.

4. Chromium as a paleoredox proxy

The utility of Cr as a paleoredox proxy is due to its contrasting solubilities in oxygen-rich and oxygen-poor environments and the distinctive isotope fractionations associated with redox transitions. Chromium occurs in igneous rocks as insoluble Cr(III), with an isotopic composition of –0.12 ± 0.10‰ δ⁵³Cr (e.g., Schoenberg et al., 2008), but can be converted to soluble Cr(VI) through reactions with manganese(IV) oxides in terrestrial weathering environments (e.g., Frei et al., 2009). Since the main pathway for Mn(IV) oxide formation requires molecular oxygen (although see Supplementary Text and Daye et al., 2019; Liu et al., 2020), and Cr(III) oxidation with Mn(IV) oxides induces a strong positive fractionation—theoretically ~ +6‰, but lower in natural environments (see references in Wei et al., 2020)—the presence of fractionated Cr in aqueous environments indirectly attests to the availability of free oxygen in the atmosphere (see Supplementary Text and Miletto et al., 2021; Saad et al., 2017 for alternative takes). Additional Cr isotope fractionations can occur during redox reactions in rivers (e.g., Ellis et al., 2002) and oceans (e.g., Miletto et al., 2021), producing δ⁵³Cr values that vary between +0.3‰ and +1.6‰ in modern seawater. Such fractionated δ⁵³Cr signals can be captured by sediments accumulating under a reducing water column that scavenge dissolved Cr, so that the presence or absence of fractionated Cr in sediments can be used to track atmospheric oxygen levels through Earth history (Frei et al., 2009; Wei et al., 2020). Similarly, since concentrations of soluble Cr(VI) in seawater scale with the generation of Mn(IV) oxides in terrestrial settings and with the abundance of oxygen-rich settings in the oceans, Cr concentration trends in anoxic sediments (which readily scavenge dissolved Cr) have also been tied to fluctuations in the extent of anoxic and euxinic seafloor area. For example, Reinhard et al. (2013) reported a shift from ~ 0.017 μg g⁻¹/μg g⁻¹ Cr/Ti ratios in mid-Proterozoic mudstones to ~ 0.05 in Neoproterozoic mudstones, corresponding to expected shifts in atmospheric oxygen levels over the Proterozoic.

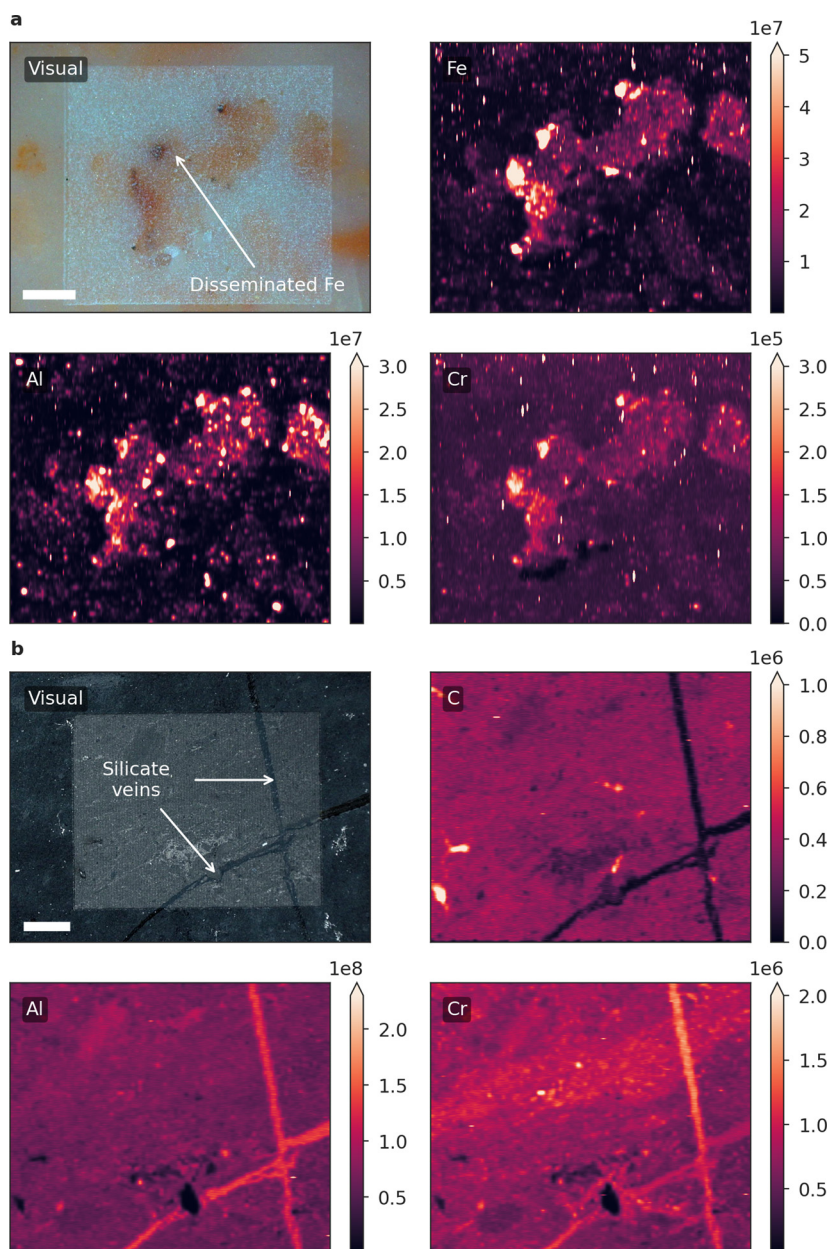


Fig. 2. In-situ element maps for representative Omega Basin samples. Optical micrographs and relative carbon, aluminum, iron, and chromium abundance maps (reported in counts per second), determined through laser-ablation mass-spectrometry from representative lithologies in the OPH core. (a) Evaporitic carbonate sample OPH-4081 (depth 2305.25 m, $\delta^{53}\text{Cr} = 1.16 \pm 0.08\text{‰}$), composed mainly of magnesite-dolomite, hosts disseminated Fe-rich phases, in which Cr is preferentially concentrated. (b) C_{org} -rich mudstone sample OPH-1572 (depth 1112.08 m, $\delta^{53}\text{Cr} = 1.63 \pm 0.11\text{‰}$) displays C_{org} -rich sedimentary laminae and Al-rich cross-cutting mica veins. Cr is concentrated both in the laminae and veins. Scale bars are 1 mm. Note difference in color scale.

Organic-rich mudstones, such as those of the Zaonega Formation, can quantitatively capture marine $\delta^{53}\text{Cr}$ due to the fast kinetics of Cr(VI) reduction in anoxic waters, as has been demonstrated in the anoxic Cariaco Basin (e.g., Reinhard et al., 2014). Carbonates, while a much less efficient sink, capture Cr with a negative fractionation in biogenic carbonates but possibly minimal fractionation in abiogenic ones (Rodler et al., 2015). Therefore, $\delta^{53}\text{Cr}$ values in Tulomozero Formation carbonates can be considered a minimum boundary on seawater values. Compared to mudstones and carbonates, evaporites are much less studied in terms of their Cr isotopic composition. Yet, existing work on groundwater-derived evaporites in the Atacama Desert suggests that Cr is captured quantitatively in chromate salts (Pérez-Fodich et al., 2014). Likewise, the presence of bittern salts in the lower Tulomozero Formation implies cycles of almost complete seawater evaporation in the basin, which strongly

support nearly quantitative capture of all seawater components. This is confirmed by element mapping of the most ^{53}Cr -enriched evaporite sample (OPH-4081, 2305.25 m depth) which shows that chromium is hosted in diffuse, likely authigenic, reddish Fe-rich phases that are disseminated throughout the magnesite-dolomite matrix (Fig. 2a).

In our Omega Basin samples, bulk Cr concentrations range between 0.3 and 2283.1 $\mu\text{g g}^{-1}$, with a median of 86.1 $\mu\text{g g}^{-1}$ ($n = 253$). Authigenic Cr abundances, expressed as Cr/Ti (Cole et al., 2017), range between 0.002 and 0.694 ($\mu\text{g g}^{-1}/\mu\text{g g}^{-1}$; Fig. 3), with a median of 0.039 ($n = 253$). Due to different Cr drawdown affinities of different lithologies (see Methods for classification), the median Cr/Ti value in Tulomozero Formation evaporites is 0.075 (range 0.002–0.366; $n = 16$); in Tulomozero and Zaonega Formation carbonates, 0.040 (range 0.008–0.694; $n = 93$); and in mud-

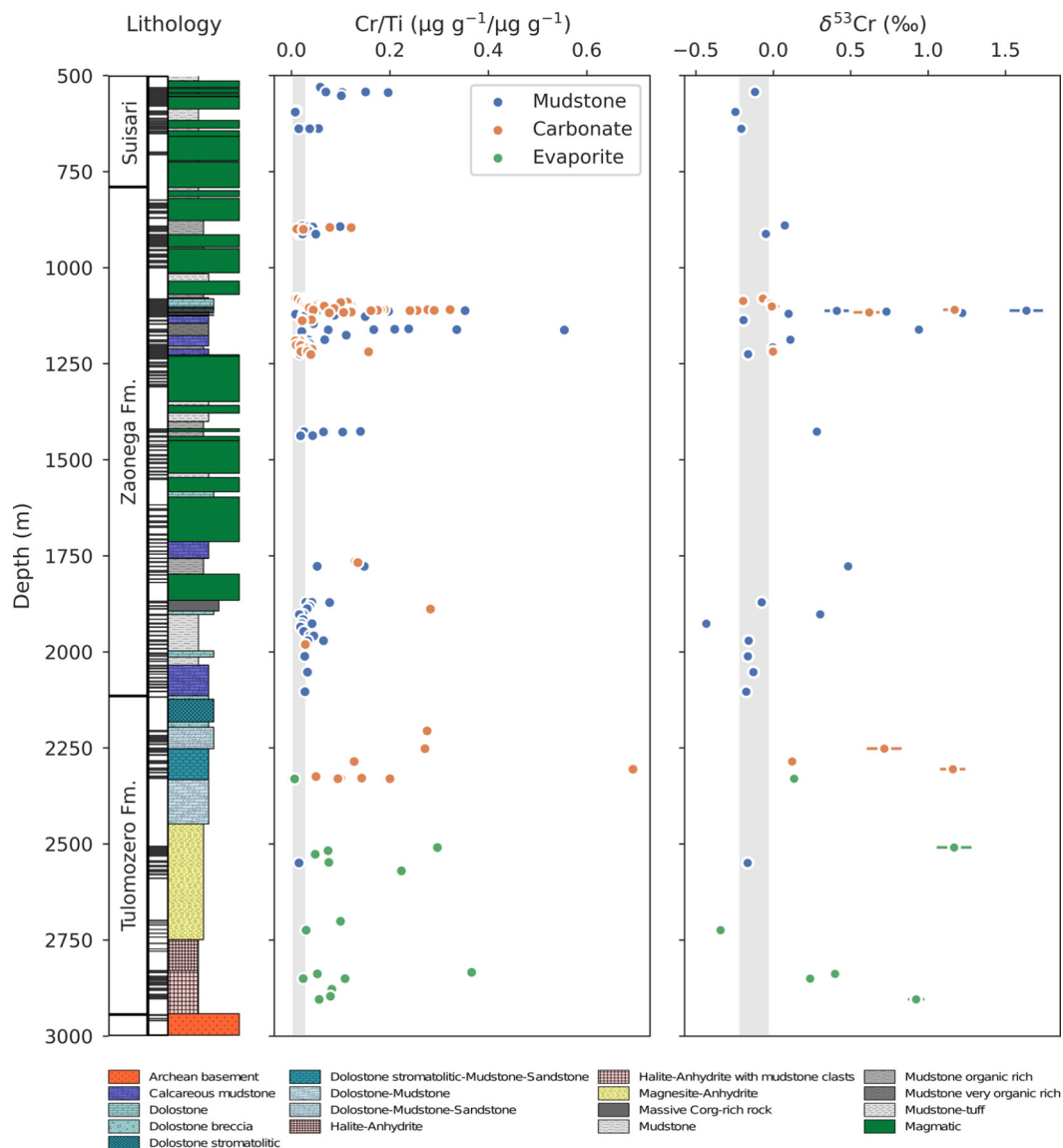


Fig. 3. Chromium geochemistry in the Omega Parametric Hole drill core. Columns show the lithology, abundance of authigenic chromium (Cr/Ti), and its isotopic composition ($\delta^{53}\text{Cr}$). Color of datapoints corresponds to lithology. Crustal averages, vertical gray bars, are taken from Cole et al. (2017) and Schoenberg et al. (2008).

stones throughout the succession, 0.037 (range 0.003–0.554; $n = 144$). Significantly fractionated $\delta^{53}\text{Cr}$ values are present throughout the entire studied section, varying between $-0.43 \pm 0.03\text{‰}$ and $+1.64 \pm 0.10\text{‰}$ $\delta^{53}\text{Cr}$ (errors are 2σ), with an average of $+0.24\text{‰}$ ($n = 41$; Fig. 3). In evaporites, $\delta^{53}\text{Cr}$ ranges between -0.34 and $+1.17\text{‰}$ (average $+0.42\text{‰}$; $n = 6$); in dolostones, between -0.20 and $+1.17\text{‰}$ (average $+0.20\text{‰}$; $n = 14$); and in mudstones, from -0.43 to $+1.64\text{‰}$ (average $+0.22\text{‰}$; $n = 21$) (Fig. 4). These values, being the highest reported so far for the Paleoproterozoic (Reinhard et al., 2013; Wei et al., 2020), are difficult to explain through currently known oxygen-independent processes. For instance, ligand-based Cr(III) solubilization occurs at significantly lower rates than proton-driven solubilization (Saad et al., 2017), UV-based Mn(II) photo-oxidation was, by the time of the middle Paleoproterozoic, hampered by the ozone layer (Liu et al., 2020), and Mn(IV) oxides produced through anoxygenic photosynthesis in reduced surface settings (Daye et al., 2019) would have been vulnerable to back-reduction prior to diffusing to subsurface Cr weathering environments (Anbar and Holland, 1992). Therefore, the data most likely reflect elevated redox potentials during the

deposition of the Tulomozero and Zaonega formations (see Supplementary Text for more discussion on alternatives).

5. Post-depositional alteration of chromium

Due to its complex geological history, secondary processes within the Omega Basin succession may have altered some geochemical signals. For example, stromatolitic carbonates in the Tulomozero Formation have undergone pervasive dolomite/magnesite recrystallization with micritic fabrics being destroyed, but most samples have retained recognizable bedding and lamination (Melezhik et al., 2015, 1999). Zaonega Formation carbonates, where dolomite is the primary phase, have in large part been secondarily de-dolomitized to calcite, with a concomitant decrease in both their $\delta^{18}\text{O}$ and $\delta^{13}\text{C}$ values, though this has primarily affected the margins of dolomite beds (Kreitsmann et al., 2019). Furthermore, there are pervasive quartz-mica veins in the mudstones of the Zaonega Formation that were emplaced due to syn-depositional hydrothermal activity triggered by the emplacement of mafic lavas and sills or during later greenschist facies metamorphism (Paiste et al., 2018). Elemental mapping of the most ^{53}Cr -enriched mudstone sample (OPH-1572, 1112.08 m depth) shows

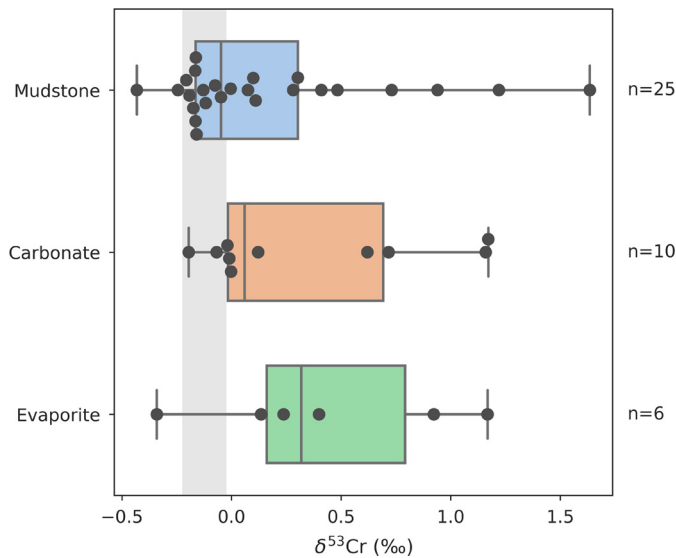


Fig. 4. Chromium isotope ratios per lithology. Boxplots show medians, 25/75th quantiles, and the full range; superimposed black circles are individual samples. Grey bar denotes average crustal composition from Schoenberg et al. (2008).

that Cr is enriched both in C_{org} -rich laminae, as well as in microscale mica veins, suggesting some Cr mobilization into percolating fluids (Fig. 2b).

Despite the evidence above for post-depositional fluid alteration, several factors suggest that this process cannot explain the positively fractionated $\delta^{53}\text{Cr}$ values in the Onega Basin. First, conspicuous veins, mono-mineral clusters, and altered margins of carbonate beds were carefully screened and avoided during sample selection. Second, igneous-derived Cr from hydrothermal sources is expected to host negative or crustal $\delta^{53}\text{Cr}$ ratios (Schoenberg et al., 2008), and remobilization of primary Cr(III) is likely to drive residual sediment $\delta^{53}\text{Cr}$ values more negative (Ellis et al., 2002), yet our samples have positive $\delta^{53}\text{Cr}$ values. The lack of alteration is also evident by Cr mapping—concentrations in mica veins are highest in the areas where they cross Cr-rich laminae (Fig. 2b), suggesting adjacent laminae as the source of Cr. Finally, the evaporite section of the lower Tulomozero Formation is composed of minerals, such as halite and bittern salts, which are highly susceptible to fluid alteration. Their persistence implies that substantial fluid movement has not occurred in these rocks.

Carbonates in the Onega Basin deserve further assessment since this lithology has a high propensity for diagenetic recrystallization. Oxygen isotope values provide a means of tracking the influence of diagenetic processes, given that more pervasive diagenesis typically leads to lower $\delta^{18}\text{O}$ values (Klaebe et al., 2021, and references therein). Carbonate $\delta^{18}\text{O}$ values in our Onega Basin samples range between -17.2 and -4.8‰ , with an average of $-11.0 \pm 2.7\text{‰}$ (VPDB; $n = 45$; Fig. S1). However, Fig. 5 shows that the samples with the highest $\delta^{18}\text{O}$ values, hence being the ‘least altered’, tend to have more fractionated Cr compositions than those with low $\delta^{18}\text{O}$ values, suggesting, in the standard framework, that secondary processes likely decreased, not increased $\delta^{53}\text{Cr}$ values (cf. Klaebe et al., 2021).

Another illustration that Cr geochemistry in the Onega Basin reflects primary processes is Fig. 6a, which relates Cr/Ti to $\delta^{53}\text{Cr}$ in all three lithologies. That nearly all samples lie on a general positive trend suggests that $\delta^{53}\text{Cr}$ variance throughout the Onega Basin can largely be explained through the mixing of two components—an unfractionated detrital source and a fractionated seawater source (e.g., Planavsky et al., 2014)—without needing to invoke secondary overprint.

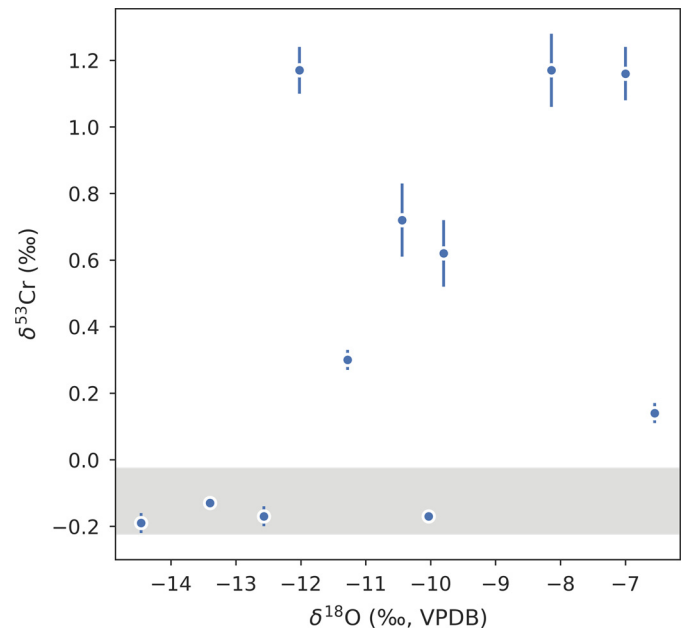


Fig. 5. Relationships between chromium and oxygen isotope ratios in carbonates. Chromium isotope ratios ($\delta^{53}\text{Cr}$) are plotted against oxygen isotope ratios ($\delta^{18}\text{O}$ VPDB); in the latter case, lower values are indicative of stronger alteration of carbonates. Grey bar denotes average crustal composition from Schoenberg et al. (2008).

6. Basin controls on the dissolved chromium pool

Even if the authigenic $\delta^{53}\text{Cr}$ reflects a seawater signal, it is possible that elevated $\delta^{53}\text{Cr}$ was only a local phenomenon, and not representative of global Cr cycling. There is strong evidence for basin restriction in the Onega Basin that would allow such a scenario—evaporite mineralogy and sedimentary textures indicative of shallow deposition abound in the Tulomozero Formation (Blättler et al., 2018; Melezhik et al., 1999). Furthermore, the sulfur and iron isotope records in the Zaonega Formation have been interpreted to reflect varying levels of restriction (Mänd et al., 2021; Paiste et al., 2020b). In this case, distillation of the dissolved Cr pool by preferential drawdown of ^{52}Cr (i.e., Rayleigh fractionation) could have driven $\delta^{53}\text{Cr}$ more positive. Alternatively, positive values may have resulted from an anomalously positive riverine source of Cr.

However, Cr concentrations consistently reach hundreds of $\mu\text{g g}^{-1}$ over the hundreds of meters of mudstone-carbonate stratigraphy in the Zaonega and Suisari formations making it unlikely that a single point source could have provided this Cr. Distillation of the Cr pool is also unlikely, as that implies a substantial diminution of the dissolved Cr—it is far more parsimonious to invoke a fractionated open marine Cr source (e.g., Mänd et al., 2020). Conversely, in the lower Tulomozero Formation, the precipitation of a thick evaporite succession including bittern salts implies that seawater evaporation and Cr drawdown likely proceeded nearly to completion during numerous evaporative cycles (Blättler et al., 2018), again precluding a distillation effect on the $\delta^{53}\text{Cr}$ signal. While the shallow-water upper Tulomozero Formation carbonates present the highest likelihood of $\delta^{53}\text{Cr}$ distillation, the low efficiency of Cr incorporation into carbonates (Reinhard et al., 2013) again precludes strong distillation.

Variable Cr abundances and isotope ratios attest to differences in Cr cycling and drawdown across the Onega Basin succession (Fig. 3). For example, the highest Cr/Ti ratios (up to 0.353) and $\delta^{53}\text{Cr}$ values (up to 1.64‰) are consistently present in the ~ 1115 – 1108 m interval that hosts a distinctive P-rich mudstone-dolostone contact—a marker horizon within the Onega

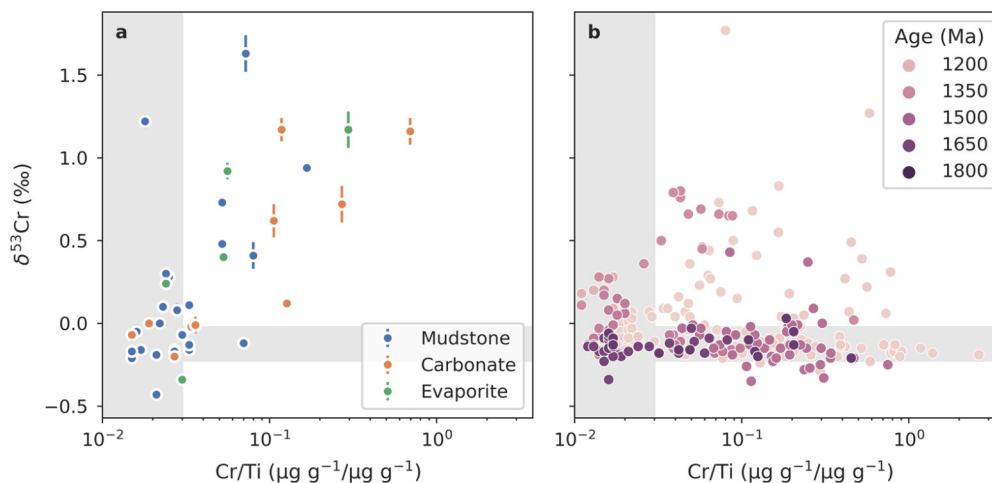


Fig. 6. Authigenic chromium abundances (Cr/Ti) plotted against isotope ratios ($\delta^{53}\text{Cr}$). (a) Omega Basin data from this study, colored per lithology. (b) Published data from mid-Proterozoic sections of various lithologies, colored according to age (1950–1000 Ma). A positive trend, as opposed to a horizontal one, suggests Cr(VI) cycling and the presence of atmospheric oxygen (e.g., Planavsky et al., 2014). Data for panel b is from Frei and Polat (2013), Planavsky et al. (2014), Cole et al. (2016), Gilleaudeau et al. (2016), Canfield et al. (2018), and Wei et al. (2021).

Basin (Paiste et al., 2020a). This same interval displays extremely high TOC content (up to > 70 wt.%), authigenic apatite, and fossilized sulfur cycling microbial ecosystems which are interpreted as having been formed in a highly biologically productive setting with fluctuating sulfidic–suboxic redox boundaries close to sediment surface that are especially conducive to redox-sensitive metal drawdown (Lepland et al., 2014; Mänd et al., 2020). Additionally, since the interval was host to a degree of hydrocarbon migration (Qu et al., 2012), secondary Cr accumulation may have contributed to these maximum values (though as a high-temperature process, this is unlikely to have caused isotope fractionations). On the other hand, marl samples from the transition zone of the Tulomozero and Zaonega formations (between 2100–1920 m) and in the Suisari Formation (above 640 m) host unfractionated Cr ($\delta^{53}\text{Cr}$ below -0.13‰ and -0.12‰ , respectively) at low authigenic concentrations (Cr/Ti below 0.065 and 0.196, respectively). In these latter cases, high levels of plagioclase (up to 53.2%), and the presence of amphibole and titanite, suggest that the sediments may have experienced substantial volcanic ash input that delivered unfractionated, igneous Cr. Since almost all samples lie on a generally positive trend between $\delta^{53}\text{Cr}$ and Cr/Ti (Fig. 6a), variation in both of these parameters can be sufficiently explained through variable Cr drawdown efficiencies or detrital input, leading to differing ratios of authigenic to detrital Cr. While it remains possible that waters in the Omega Basin experienced basin-specific Cr cycling, the presence of substantial volumes of isotopically fractionated Cr demand an oxygenated ocean–atmospheric system that can host Cr(VI)-cycling.

7. Atmospheric–oceanic redox in the Paleoproterozoic

The Rhyacian period has been proposed as a time of elevated oxygen abundance in the middle Paleoproterozoic, potentially sandwiched between times of comparatively lower oxygen abundance (Bekker and Holland, 2012). Oxygenated conditions are evidenced by evaporite mineralogy together with calcium and sulfur isotope records that indicate elevated marine sulfate levels (Blättler et al., 2018), consistent with high redox-sensitive element concentrations and isotope ratios (see references in Robbins et al., 2016). This period of O_2 abundance was originally tied to the Lomagundi–Jatuli carbon isotope excursion through the mechanism of excess organic carbon burial (Bekker and Holland, 2012; Karhu and Holland, 1996), although this interpretation has become increasingly challenged (e.g., Mänd et al., 2020).

Intriguingly, the Rhyacian rock record is characterized by very minor sedimentary Cr isotope anomalies, despite this proxy being frequently cited as evidence for atmospheric oxygenation (Wei et al., 2020). Previous reports of positively fractionated Cr in the Paleoproterozoic do exist (Fig. 7), particularly in the ~ 1.85 Ga Gunflint iron formation (Fralick et al., 2017; Frei et al., 2009), coupled with subtly negatively fractionated Cr in the ~ 1.9 Ga Schreiber Beach paleosol (Frei and Polat, 2013), both consistent with Cr(VI) solubilization and transport to the oceans. However, with the exception of meteorically derived diagenetic carbonate cements in the Gunflint Formation (Fralick et al., 2017), these fractionations barely extend beyond the crustal mean (maximum of $+0.21\text{‰}$), and are even surpassed by $\delta^{53}\text{Cr}$ data from the Neoproterozoic that are indicative of relatively minor amounts of Cr(IV) weathering and cycling in a predominantly anoxic world (Frei et al., 2009). Furthermore, $\delta^{53}\text{Cr}$ values of Rhyacian iron formations are even less fractionated (up to $+0.03\text{‰}$) (Frei et al., 2009). The anomalous feature of the later Paleoproterozoic $\delta^{53}\text{Cr}$ record is high positive fractionations (up to $+2.34\text{‰}$) in the ~ 1.9 Ga Flin Flon and Beaverlodge Lake paleosols (Babechuk et al., 2017; Toma et al., 2019), which constitute the opposite of the expected isotope effect of oxic Cr weathering and have, thus, been linked to redox-independent Cr solubilization, instead of oxidative Cr cycling (e.g., Konhauser et al., 2011).

Collectively, these data have been used to suggest a late Paleoproterozoic to Mesoproterozoic Cr cycle highly distinct from the modern—variable atmospheric $p\text{O}_2$ produced, potentially in an alternating fashion, localized positively fractionated Cr runoff related to Mn(IV) oxide cycling (Fralick et al., 2017; Frei and Polat, 2013) or negatively fractionated runoff related to ligand- or acid-based solubilization (Babechuk et al., 2017; Toma et al., 2019). The oceans, meanwhile, are implied to have remained predominantly anoxic, with relatively minor fractionated Cr runoff diluted within an unfractionated marine reservoir.

In contrast to this mid-Proterozoic scenario, illustrated by a general lack of correlation between Cr/Ti and $\delta^{53}\text{Cr}$ at this time (Fig. 6b), our data from the ~ 2.1 – 2.0 Ga Omega Basin suggest a modern-type Cr cycle in the Rhyacian to the early Orosirian: nearly all samples follow a positive trend between Cr/Ti and $\delta^{53}\text{Cr}$ (Fig. 6a) that is a telltale sign of oxidative Cr(VI) cycling coupled to Mn(II) oxidation (Planavsky et al., 2014). Whereas Fe(II) oxidation occurs at circumneutral pH at near 0 mV potential, high-potential redox reactions ($\gg 500$ mV) are required to oxidize Mn(II) under the same conditions. Although it remains unresolved how much,

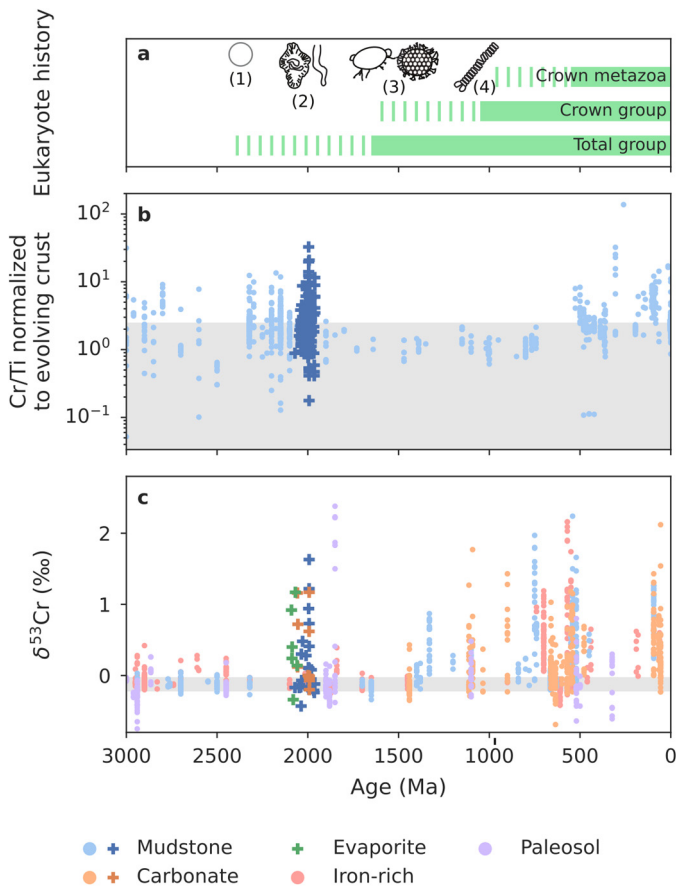


Fig. 7. The early record of eukaryotes and other possible complex life (a), authigenic chromium abundances (using Cr/Ti as proxy) in shales (b), and $\delta^{53}\text{Cr}$ values in various geological archives (c) through time. Cartoons in (a) represent (1) an idealized early stem eukaryote lacking preservable, diagnostically eukaryotic features; (2) puzzling structures that might represent extinct eukaryote-grade life, including macroscopic pyrite structures with radial fabric (left) and macroscopic trails (right) (El Albani et al., 2010; Rasmussen et al., 2002; Bengtson et al., 2007); (3) the oldest widely accepted evidence for total group eukaryotes, including the organic-walled microfossil *Tappania plana* (left) and *Shuiyosphaeridium macroreticulatum* (right) (e.g., Miao et al., 2019; Javaux et al., 2001; Agić et al., 2015); and (4) the oldest fossil evidence for crown group eukaryotes (e.g., *Bangiomorpha pubescens*; Butterfield, 2000). Age ranges for the origin of total group eukaryotes are taken from Betts et al. (2018) (max age) and Miao et al. (2019) (minimum age); and for the origin of crown group eukaryotes from Parfrey et al. (2011) and Eme et al. (2014) (maximum age) and Butterfield (2000) and Gibson et al. (2018) (minimum age). Crown group metazoa ages are from Love et al. (2009), Sperling and Stockey (2018) and Turner (2021) (maximum age) and Xiao and Laflamme (2009) (minimum age). Differently colored pastel dots on panels b and c represent previously published data of different lithological affinities. Saturated cross symbols are data from this study. Cr/Ti data is from Reinhard et al. (2013) and Robbins et al. (2016); $\delta^{53}\text{Cr}$ data is from the compilation of Wei et al. (2020) and Wei et al. (2021). Since Cr concentrations in the crust have decreased through geological time due to a decreasing prevalence of Cr-rich ultramafic igneous rocks, samples have been normalized to changes in crustal abundance according to Condie (1993). Grey bars represent average crustal compositions as in Fig. 2. Errors are smaller than the data symbols.

and for how long, oxygen levels would have to rise above $\sim 0.1\text{--}1\%$ of the present atmospheric level (PAL), as is required for substantial Mn(IV)-driven Cr(III) oxidation without quantitative Cr(VI) back-reduction by Fe(II) phases (Planavsky et al., 2014), highly fractionated $\delta^{53}\text{Cr}$ values coupled to high authigenic Cr enrichments imply globally elevated $p\text{O}_2$ levels (see discussion on alternative Mn oxidation and Cr fractionation mechanisms in Supplementary Text). This Cr(VI) then accumulated in relatively oxygen-replete oceans, where the oxyanion was stable. The large, positively fractionated marine Cr pool was then further subjected to biochemical Cr redox cycling in the photic zone (e.g., Miletto et al., 2021).

Our key finding is that, despite downcore variability in magnitude, the fractionated $\delta^{53}\text{Cr}$ values persist for nearly the entirety of the $\sim 2400\text{-m}$ -thick sampled succession, across facies that transition from a shallow evaporative setting to a deeper water turbidite system, and most likely representing several tens to potentially more than a hundred Myrs of time (Figs. 3, 7). Most parsimoniously, the data suggest that Earth's atmospheric oxygenation remained above the $\sim 0.1\text{--}1\%$ $p\text{O}_2$ threshold for Cr(III) oxidation and transport to the oceans (Planavsky et al., 2014) for the entirety of this time period. These findings provide a striking contrast to what are increasingly seen as highly variable mid-Proterozoic redox conditions (e.g., Tang et al., 2017). In this light, the Orosirian period perhaps witnessed a momentous transition from a well redox buffered to a poorly-buffered atmospheric–oceanic redox state. This provides support for recent triple O isotope studies that suggest elevated bioproductivity and O_2 production in the middle Paleoproterozoic (Crockford et al., 2018), possibly due to increased nutrient fluxes (Konhauser et al., 2011; Bekker and Holland, 2012).

8. Implications for the evolution of biological complexity

Oxygen is often cited as the most important factor modulating the evolution and diversification of complex life on our planet, driving, for example, increases in body size through time, the diversification of eukaryotes, the origin of animals, and ultimately the invasion of land by vertebrates and arthropods (e.g., Falkowski et al., 2005; Ward et al., 2006; Berner et al., 2007; Payne et al., 2009; Sperling et al., 2013; Knoll, 2014; Planavsky et al., 2014; Cole et al., 2020). More difficult to assess is the connection between oxygen and the origin of complex cells, in particular, the eukaryotic cell, with its organelles, endomembrane system, relatively large size, and sophisticated cytoskeleton. It is reasonable to suggest that free oxygen is a necessary precondition for the evolution of crown group eukaryotes—the clade comprising the last common ancestor of all living eukaryotes (LECA) and all of its descendants—given that LECA possessed mitochondria and, presumably, sterols (Desmond and Gribaldo, 2009), both of which would have required oxygen, albeit at very low levels (Waldbauer et al., 2011) or, possibly, only intermittently (Müller et al., 2012). But it is an open question whether an increase in oxygen was the driver for the origin of crown group eukaryotes—whether very low oxygen levels acted as a brake, that, once released, resulted in the immediate, or at least inevitable, evolution of cellular complexity.

One challenge in answering this question is that it is hard to pin down when the complex cells of eukaryotes evolved. In part this is because much of early eukaryotic evolution probably occurred in species that would not have been preserved, or, if preserved, would not have exhibited preservable characters that would allow us to recognize them as eukaryotes. Molecular clock studies permit the possibility that stem group eukaryotes emerged in the early Paleoproterozoic (e.g., Betts et al., 2018; Gold et al., 2017), but by definition these first eukaryotes would not have possessed any of the complex traits that characterize crown group eukaryotes; they would have been nearly or completely indistinguishable from their prokaryotic relatives (Porter, 2020). Rocks younger than 1700 Ma (Agić et al., 2015, 2017; Adam et al., 2017; Javaux et al., 2001; Javaux and Knoll, 2017) preserve fossils that indicate that eukaryotes had evolved a sophisticated cytoskeleton, the ability to form resistant organic walls, and, possibly, a Golgi apparatus and endomembrane system (Javaux and Knoll, 2017), but whether other traits like mitochondria and the nucleus were present by this time—or had evolved long before—is not clear. Molecular clock estimates for LECA are wide ranging (Porter, 2020), and, in any case, only provide minimum age constraints for the origin of complex cells: an age of 1.8 Ga for LECA, for example, does not tell us whether the nucleus, sophisticated cytoskeleton, and mitochon-

dria were present much earlier (see Shih and Matzke, 2013 for a younger age estimate for the last of these). Thus, we do not know when complex eukaryotic cells emerged. Furthermore, even if we were able to constrain the timing of their origin to an interval when oxygen levels increased, it is still difficult to assess a causal connection given that it's a single biological event (and therefore a just-so story). More robust evidence would be multiple independent acquisition of complex cells across numerous clades associated with a rise in oxygen (Butterfield, 2009). But just as with the early eukaryotic fossil record, it seems likely that if other, now-extinct lineages had evolved complex, eukaryote-grade cells, they would not be easily preserved, or if preserved, they would be difficult to recognize as such. In fact, it is worth considering whether some of the puzzling structures reported from Paleoproterozoic rocks could represent these extinct lineages (e.g., El Albani et al., 2010, 2019; Rasmussen et al., 2002; Bengtson et al., 2007).

What we can say, however, is that if there had been a delay in the appearance of complex cells—if complex eukaryotic cells did in fact arise ca. 1.7 Ga or later, and not ca. 2.1 Ga—it is unlikely to be due to a lack of oxygen. Results from the Onega Basin indicate that oxygen levels were high enough and stable enough to support modern eukaryotic life for tens to > 100 million years, from at least 2.1 to 2.0 Ga and perhaps earlier. Thus, if there was a delay, then we are forced to seek other reasons to explain it. Maybe other physical or ecological barriers prevented the evolution of complex cells during the Paleoproterozoic; maybe oxygen was an important driver but it simply takes a very long time for complex cells to evolve—longer than the tens to > 100 million years recorded in the Onega Basin; or maybe the evolution of cellular complexity is not an inevitable result of rising oxygen (or any other environmental factor). In the case of the latter, the appearance of complex life on this planet might reflect, in large part, a series of contingent events.

CRediT authorship contribution statement

Kaarel Mänd: Conceptualization, Formal analysis, Investigation, Writing – original draft. **Noah J. Planavsky:** Conceptualization, Investigation, Methodology, Resources, Validation, Writing – review & editing. **Susannah M. Porter:** Conceptualization, Validation, Writing – original draft, Writing – review & editing. **Leslie J. Robbins:** Formal analysis, Investigation, Validation, Writing – review & editing. **Change Wang:** Formal analysis, Investigation, Validation, Writing – review & editing. **Timmu Kreitsmann:** Investigation, Validation, Writing – review & editing. **Kärt Paiste:** Investigation, Validation, Writing – review & editing. **Päärn Paiste:** Formal analysis, Investigation, Methodology, Validation, Writing – review & editing. **Alexander E. Romashkin:** Investigation, Resources. **Yulia E. Deines:** Investigation, Resources, Writing – review & editing. **Kalle Kirsimäe:** Conceptualization, Formal analysis, Investigation, Methodology, Resources, Validation, Writing – review & editing. **Aivo Lepland:** Conceptualization, Investigation, Resources, Validation, Writing – review & editing. **Kurt O. Konhauser:** Conceptualization, Investigation, Resources, Validation, Writing – original draft, Writing – review & editing.

Declaration of competing interest

The authors declare that they have no known competing financial interests or personal relationships that could have appeared to influence the work reported in this paper.

Acknowledgements

We would like to thank Roger Buick, Nicholas J. Butterfield, Emmanuelle J. Javaux, two anonymous reviewers, and the edi-

tor Boswell Wing for discussions that significantly improved the manuscript.

Funding: Ministry of Education and Research of Estonia, The Kristjan Jaak Scholarship program (KM); UAlberta North, Ashley & Janet Cameron Graduate Scholarship (KM); Estonian Research Council grant PRG447 (KM, TK, KK); Natural Sciences and Engineering Research Council of Canada Discovery grant RGPIN-165831 (KOK); European Union's Horizon 2020 Research and Innovation Programme, Marie Skłodowska-Curie grant agreement No. 894831 (KP).

Appendix A. Supplementary material

Supplementary material related to this article can be found online at <https://doi.org/10.1016/j.epsl.2022.117501>.

References

- Adam, Z.R., Skidmore, M.L., Mogk, D.W., Butterfield, N.J., 2017. A Laurentian record of the earliest fossil eukaryotes. *Geology* 45, 387–390. <https://doi.org/10.1130/G38749.1>.
- Agić, H., Moczyłowska, M., Yin, L.-M., 2015. Affinity, life cycle, and intracellular complexity of organic-walled microfossils from the Mesoproterozoic of Shanxi, China. *J. Paleontol.* 89, 28–50. <https://doi.org/10.1017/jpa.2014.4>.
- Agić, H., Moczyłowska, M., Yin, L., 2017. Diversity of organic-walled microfossils from the early Mesoproterozoic Ruyang Group, North China Craton—a window into the early eukaryote evolution. *Precambrian Res.* 297, 101–130. <https://doi.org/10.1016/j.precamres.2017.04.042>.
- Amelin, Yu.V., Heaman, L.M., Semenov, V.S., 1995. U-Pb geochronology of layered mafic intrusions in the eastern Baltic Shield: implications for the timing and duration of Paleoproterozoic continental rifting. *Precambrian Res.* 75, 31–46. [https://doi.org/10.1016/0301-9268\(95\)00015-W](https://doi.org/10.1016/0301-9268(95)00015-W).
- Anbar, A.D., Holland, H.D., 1992. The photochemistry of manganese and the origin of banded iron formations. *Geochim. Cosmochim. Acta* 56, 2595–2603. [https://doi.org/10.1016/0016-7037\(92\)90346-K](https://doi.org/10.1016/0016-7037(92)90346-K).
- Babechuk, M.G., Kleinhanns, I.C., Schoenberg, R., 2017. Chromium geochemistry of the ca. 1.85 Ga Flin Flon paleosol. *Geobiology* 15, 30–50. <https://doi.org/10.1111/gbi.12203>.
- Bauer, A.M., Rooney, A.D., Lepland, A., Cole, D.B., Planavsky, N.J., 2019. The dynamics of the Lomagundi–Jatuli carbon isotope excursion and implications for early life. In: *Geobiology 2019 Conference Proceedings*. Presented at the 2nd Geobiology Society Conference, Banff, Canada.
- Bekker, A., Holland, H.D., 2012. Oxygen overshoot and recovery during the early Paleoproterozoic. *Earth Planet. Sci. Lett.* 317–318, 295–304. <https://doi.org/10.1016/j.epsl.2011.12.012>.
- Bellefroid, E.J., Hood, A.V.S., Hoffman, P.F., Thomas, M.D., Reinhard, C.T., Planavsky, N.J., 2018. Constraints on Paleoproterozoic atmospheric oxygen levels. *Proc. Natl. Acad. Sci. USA* 115, 8104–8109. <https://doi.org/10.1073/pnas.1806216115>.
- Bengtson, S., Rasmussen, B., Krapež, B., 2007. The Paleoproterozoic megascopic Stirling biota. *Paleobiology* 33, 351–381. <https://doi.org/10.1017/S0094837300026348>.
- Berner, R.A., VandenBrooks, J.M., Ward, P.D., 2007. Oxygen and evolution. *Science* 316, 557–558. <https://doi.org/10.1126/science.1140273>.
- Betts, H.C., Puttick, M.N., Clark, J.W., Williams, T.A., Donoghue, P.C.J., Pisani, D., 2018. Integrated genomic and fossil evidence illuminates life's early evolution and eukaryote origin. *Nat. Ecol. Evol.* 2, 1556. <https://doi.org/10.1038/s41559-018-0644-x>.
- Blättler, C.L., Claire, M.W., Prave, A.R., Kirsimäe, K., Higgins, J.A., Medvedev, P.V., Romashkin, A.E., Rychanchik, D.V., Zerkle, A.L., Paiste, K., Kreitsmann, T., Millar, I.L., Hayles, J.A., Bao, H., Turchyn, A.V., Warke, M.R., Lepland, A., 2018. Two-billion-year-old evaporites capture Earth's great oxidation. *Science* 360, 320–323. <https://doi.org/10.1126/science.aar2687>.
- Butterfield, N.J., 2009. Oxygen, animals and oceanic ventilation: an alternative view. *Geobiology* 7, 1–7. <https://doi.org/10.1111/j.1472-4669.2009.00188.x>.
- Butterfield, N.J., 2000. *Bangiomorpha pubescens* n. gen., n. sp.: implications for the evolution of sex, multicellularity, and the Mesoproterozoic/Neoproterozoic radiation of eukaryotes. *Paleobiology* 26, 386–404. [https://doi.org/10.1666/0094-8373\(2000\)026<0386:BPNGNS>2.0.CO;2](https://doi.org/10.1666/0094-8373(2000)026<0386:BPNGNS>2.0.CO;2).
- Canfield, D.E., Zhang, S., Frank, A.B., Wang, X., Wang, H., Su, J., Ye, Y., Frei, R., 2018. Highly fractionated chromium isotopes in Mesoproterozoic-aged shales and atmospheric oxygen. *Nat. Commun.* 9, 1–11. <https://doi.org/10.1038/s41467-018-05263-9>.
- Catling, D.C., Glein, C.R., Zahnle, K.J., McKay, C.P., 2005. Why O₂ is required by complex life on habitable planets and the concept of planetary "oxygenation time". *Astrobiology* 5, 415–438. <https://doi.org/10.1089/ast.2005.5.415>.

- Cole, D.B., Mills, D.B., Erwin, D.H., Sperling, E.A., Porter, S.M., Reinhard, C.T., Planavsky, N.J., 2020. On the co-evolution of surface oxygen levels and animals. *Geobiology* 00, 1–22. <https://doi.org/10.1111/gbi.12382>.
- Cole, D.B., Reinhard, C.T., Wang, X., Gueguen, B., Halverson, G.P., Gibson, T., Hodgskiss, M.S.W., McKenzie, N.R., Lyons, T.W., Planavsky, N.J., 2016. A shale-hosted Cr isotope record of low atmospheric oxygen during the Proterozoic. *Geology* 44, 555–558. <https://doi.org/10.1130/G37787.1>.
- Cole, D.B., Zhang, S., Planavsky, N.J., 2017. A new estimate of detrital redox-sensitive metal concentrations and variability in fluxes to marine sediments. *Geochim. Cosmochim. Acta* 215, 337–353. <https://doi.org/10.1016/j.gca.2017.08.004>.
- Colwyn, D.A., Sheldon, N.D., Maynard, J.B., Gaines, R., Hofmann, A., Wang, X., Gueguen, B., Asael, D., Reinhard, C.T., Planavsky, N.J., 2019. A paleosol record of the evolution of Cr redox cycling and evidence for an increase in atmospheric oxygen during the Neoproterozoic. *Geobiology* 17, 579–593. <https://doi.org/10.1111/gbi.12360>.
- Condie, K.C., 1993. Chemical composition and evolution of the upper continental crust: contrasting results from surface samples and shales. *Chem. Geol.* 104, 1–37. [https://doi.org/10.1016/0009-2541\(93\)90140-E](https://doi.org/10.1016/0009-2541(93)90140-E).
- Crockford, P.W., Hayles, J.A., Bao, H., Planavsky, N.J., Bekker, A., Fralick, P.W., Halverson, G.P., Bui, T.H., Peng, Y., Wing, B.A., 2018. Triple oxygen isotope evidence for limited mid-Proterozoic primary productivity. *Nature* 559, 613–616. <https://doi.org/10.1038/s41586-018-0349-y>.
- Daye, M., Klepac-Ceraj, V., Pajusalu, M., Rowland, S., Farrell-Sherman, A., Beukes, N., Tamura, N., Fournier, G., Bosak, T., 2019. Light-driven anaerobic microbial oxidation of manganese. *Nature* 576, 311–314. <https://doi.org/10.1038/s41586-019-1804-0>.
- Desmond, E., Gribaldo, S., 2009. Phylogenomics of sterol synthesis: insights into the origin, evolution, and diversity of a key eukaryotic feature. *Genome Biol. Evol.* 1, 364–381. <https://doi.org/10.1093/gbe/evp036>.
- El Albani, A., Bengtson, S., Canfield, D.E., Bekker, A., Macchiarelli, R., Mazurier, A., Hammarlund, E.U., Boulvais, P., Dupuy, J.-J., Fontaine, C., Fürsich, F.T., Gauthier-Lafaye, F., Janvier, P., Javaux, E., Ossa, F.O., Pierson-Wickmann, A.-C., Riboulleau, A., Sardini, P., Vachard, D., Whitehouse, M., Meunier, A., 2010. Large colonial organisms with coordinated growth in oxygenated environments 2.1 Gyr ago. *Nature* 466, 100–104. <https://doi.org/10.1038/nature09166>.
- El Albani, A., Mangano, M.G., Buatois, L.A., Bengtson, S., Riboulleau, A., Bekker, A., Konhauser, K., Lyons, T., Rollion-Bard, C., Bankole, O., Baghekema, S.G.L., Meunier, A., Trentesaux, A., Mazurier, A., Aubineau, J., Laforest, C., Fontaine, C., Recourt, P., Fru, E.C., Macchiarelli, R., Reynaud, J.Y., Gauthier-Lafaye, F., Canfield, D.E., 2019. Organism motility in an oxygenated shallow-marine environment 2.1 billion years ago. *Proc. Natl. Acad. Sci.* 116, 3431–3436. <https://doi.org/10.1073/pnas.1815721116>.
- Ellis, A.S., Johnson, T.M., Bullen, T.D., 2002. Chromium isotopes and the fate of hexavalent chromium in the environment. *Science* 295, 2060–2062. <https://doi.org/10.1126/science.1068368>.
- Eme, L., Sharpe, S.C., Brown, M.W., Roger, A.J., 2014. On the age of Eukaryotes: evaluating evidence from fossils and molecular clocks. *Cold Spring Harb Perspect Biol* 6, a016139. <https://doi.org/10.1101/cshperspect.a016139>.
- Falkowski, P.G., Katz, M.E., Milligan, A.J., Fennel, K., Cramer, B.S., Aubry, M.P., Berner, R.A., Novacek, M.J., Zapol, W.M., 2005. The rise of oxygen over the past 205 million years and the evolution of large placental mammals. *Science* 309, 2202–2204. <https://doi.org/10.1126/science.1116047>.
- Farquhar, J., Bao, H., Thiemens, M., 2000. Atmospheric influence of Earth's earliest sulfur cycle. *Science* 289, 756–758. <https://doi.org/10.1126/science.289.5480.756>.
- Fralick, P., Planavsky, N., Burton, J., Jarvis, I., Addison, W.D., Barrett, T.J., Brumpton, G.R., 2017. Geochemistry of Paleoproterozoic Gunflint Formation carbonate: implications for hydrosphere-atmosphere evolution. *Precambrian Res.* 290, 126–146. <https://doi.org/10.1016/j.precambres.2016.12.014>.
- Frei, R., Gaucher, C., Poulton, S.W., Canfield, D.E., 2009. Fluctuations in Precambrian atmospheric oxygenation recorded by chromium isotopes. *Nature* 461, 250–253. <https://doi.org/10.1038/nature08266>.
- Frei, R., Polat, A., 2013. Chromium isotope fractionation during oxidative weathering—implications from the study of a Paleoproterozoic (ca. 1.9 Ga) paleosol, Schreiber Beach, Ontario, Canada. *Precambrian Res.* 224, 434–453. <https://doi.org/10.1016/j.precambres.2012.10.008>.
- Gibson, T.M., Shih, P.M., Cumming, V.M., Fischer, W.W., Crockford, P.W., Hodgskiss, M.S.W., Wörndle, S., Creaser, R.A., Rainbird, R.H., Skulski, T.M., Halverson, G.P., 2018. Precise age of Bangiomorpha pubescens dates the origin of eukaryotic photosynthesis. *Geology* 46, 135–138. <https://doi.org/10.1130/G39829.1>.
- Gilleaudeau, G.J., Frei, R., Kaufman, A.J., Kah, L.C., Azmy, K., Bartley, J.K., Chernyavskiy, P., Knoll, A.H., 2016. Oxygenation of the mid-Proterozoic atmosphere: clues from chromium isotopes in carbonates. *Geochem. Perspect. Lett.*, 178–187. <https://doi.org/10.7185/geochemlet.1618>.
- Gold, D.A., Caron, A., Fournier, G.P., Summons, R.E., 2017. Paleoproterozoic sterol biosynthesis and the rise of oxygen. *Nature* 543, 420–423. <https://doi.org/10.1038/nature21412>.
- Holland, H.D., 2002. Volcanic gases, black smokers, and the great oxidation event. *Geochim. Cosmochim. Acta* 66, 3811–3826. [https://doi.org/10.1016/S0016-7037\(02\)00950-X](https://doi.org/10.1016/S0016-7037(02)00950-X).
- Javaux, E.J., Knoll, A.H., Walter, M.R., 2001. Morphological and ecological complexity in early eukaryotic ecosystems. *Nature* 412, 66–69. <https://doi.org/10.1038/35083562>.
- Javaux, E.J., Knoll, A.H., 2017. Micropaleontology of the lower Mesoproterozoic Roper Group, Australia, and implications for early eukaryotic evolution. *J. Paleontol.* 91, 199–229. <https://doi.org/10.1017/jpa.2016.124>.
- Javaux, E.J., Lepot, K., 2018. The Paleoproterozoic fossil record: implications for the evolution of the biosphere during Earth's middle-age. *Earth-Sci. Rev.* 176, 68–86. <https://doi.org/10.1016/j.earscirev.2017.10.001>.
- Jochum, K.P., Nohl, U., Herwig, K., Lammle, E., Stoll, B., Hofmann, A.W., 2005. GeoREM: a new geochemical database for reference materials and isotopic standards. *Geostand. Geoenal. Res.* 29, 333–338. <https://doi.org/10.1111/j.1751-908X.2005.tb00904.x>.
- Karhu, J.A., Holland, H.D., 1996. Carbon isotopes and the rise of atmospheric oxygen. *Geology* 24, 867–870. [https://doi.org/10.1130/0091-7613\(1996\)024<0867:CIATRO>2.3.CO;2](https://doi.org/10.1130/0091-7613(1996)024<0867:CIATRO>2.3.CO;2).
- Klaebe, R., Swart, P., Frei, R., 2021. Chromium isotope heterogeneity on a modern carbonate platform. *Chem. Geol.* 573, 120227. <https://doi.org/10.1016/j.chemgeo.2021.120227>.
- Knoll, A.H., 2014. Paleobiological perspectives on early eukaryotic evolution. *Cold Spring Harb. Perspect. Biol.* 6, a016121. <https://doi.org/10.1101/cshperspect.a016121>.
- Konhauser, K.O., Lalonde, S.V., Planavsky, N.J., Pecoits, E., Lyons, T.W., Mojzsis, S.J., Rouxel, O.J., Barley, M.E., Rosiere, C., Fralick, P.W., Kump, L.R., Bekker, A., 2011. Aerobic bacterial pyrite oxidation and acid rock drainage during the Great Oxidation Event. *Nature* 478, 369–373. <https://doi.org/10.1038/nature10511>.
- Kreitsmann, T., Kūlavir, M., Lepland, A., Paiste, K., Paiste, P., Prave, A.R., Sepp, H., Romashkin, A.E., Rychanchik, D.V., Kirsimäe, K., 2019. Hydrothermal dedolomitisation of carbonate rocks of the Paleoproterozoic Zaonega Formation, NW Russia—implications for the preservation of primary C isotope signals. *Chem. Geol.* 512, 43–57. <https://doi.org/10.1016/j.chemgeo.2019.03.002>.
- Kreitsmann, T., Lepland, A., Bau, M., Prave, A., Paiste, K., Mänd, K., Sepp, H., Martma, T., Romashkin, A.E., Kirsimäe, K., 2020. Oxygenated conditions in the aftermath of the Lomagundi–Jatuli Event: the carbon isotope and rare earth element signatures of the Paleoproterozoic Zaonega Formation, Russia. *Precambrian Res.* 347, 105855. <https://doi.org/10.1016/j.precambres.2020.105855>.
- Lepland, A., Joosu, L., Kirsimäe, K., Prave, A.R., Romashkin, A.E., Črne, A.E., Martin, A.P., Fallick, A.E., Somelar, P., Üpraus, K., Mänd, K., Roberts, N.M.W., van Zuilen, M.A., Wirth, R., Schreiber, A., 2014. Potential influence of sulphur bacteria on Paleoproterozoic phosphogenesis. *Nat. Geosci.* 7, 20–24. <https://doi.org/10.1038/NNGEO2005>.
- Liu, W., Hao, J., Elzinga, E.J., Piotrowiak, P., Nanda, V., Yee, N., Falkowski, P.G., 2020. Anoxic photogeochemical oxidation of manganese carbonate yields manganese oxide. *Proc. Natl. Acad. Sci.* 117, 22698–22704. <https://doi.org/10.1073/pnas.2002175117>.
- Love, G.D., Grosjean, E., Stalvies, C., Fike, D.A., Grotzinger, J.P., Bradley, A.S., Kelly, A.E., Bhatia, M., Meredith, W., Snape, C.E., Bowring, S.A., Condon, D.J., Summons, R.E., 2009. Fossil steroids record the appearance of Demospongiae during the Cryogenian period. *Nature* 457, 718–721. <https://doi.org/10.1038/nature07673>.
- Lyons, T.W., Diamond, C.W., Konhauser, K.O., 2020. Shedding light on manganese cycling in the early oceans. *Proc. Natl. Acad. Sci.* 117, 25960–25962. <https://doi.org/10.1073/pnas.2016447117>.
- Mänd, K., Lalonde, S.V., Paiste, K., Thoby, M., Lumiste, K., Robbins, L.J., Kreitsmann, T., Romashkin, A.E., Kirsimäe, K., Lepland, A., Konhauser, K.O., 2021. Iron isotopes reveal a benthic iron shuttle in the Palaeoproterozoic Zaonega Formation: basinal restriction, euxinia, and the effect on global palaeoredox proxies. *Minerals* 11, 368. <https://doi.org/10.3390/min11040368>.
- Mänd, K., Lalonde, S.V., Robbins, L.J., Thoby, M., Paiste, K., Kreitsmann, T., Paiste, P., Reinhard, C.T., Romashkin, A.E., Planavsky, N.J., Kirsimäe, K., Lepland, A., Konhauser, K.O., 2020. Palaeoproterozoic oxygenated oceans following the Lomagundi–Jatuli Event. *Nat. Geosci.* 13, 302–306. <https://doi.org/10.1038/s41561-020-0558-5>.
- Martin, A.P., Condon, D.J., Prave, A.R., Lepland, A., 2013. A review of temporal constraints for the Palaeoproterozoic large, positive carbonate carbon isotope excursion (the Lomagundi–Jatuli Event). *Earth-Sci. Rev.* 127, 242–261. <https://doi.org/10.1016/j.earscirev.2013.10.006>.
- Martin, A.P., Prave, A.R., Condon, D.J., Lepland, A., Fallick, A.E., Romashkin, A.E., Medvedev, P.V., Rychanchik, D.V., 2015. Multiple Palaeoproterozoic carbon burial episodes and excursions. *Earth Planet. Sci. Lett.* 424, 226–236. <https://doi.org/10.1016/j.epsl.2015.05.023>.
- Melezhik, V.A., Fallick, A.E., Brasier, A.T., Lepland, A., 2015. Carbonate deposition in the Palaeoproterozoic Onega basin from Fennoscandia: a spotlight on the transition from the Lomagundi–Jatuli to Shunga events. *Earth-Sci. Rev.* 147, 65–98. <https://doi.org/10.1016/j.earscirev.2015.05.005>.
- Melezhik, V.A., Fallick, A.E., Medvedev, P.V., Makarikhin, V.V., 1999. Extreme $^{13}\text{C}_{\text{carb}}$ enrichment in ca. 2.0 Ga magnesite–stromatolite–dolomite–red beds' association in a global context: a case for the world-wide signal enhanced by a local environment. *Earth-Sci. Rev.* 48, 71–120. [https://doi.org/10.1016/S0012-8252\(99\)00044-6](https://doi.org/10.1016/S0012-8252(99)00044-6).
- Melezhik, V.A., Medvedev, P.V., Svetov, S.A., 2013. The Onega Basin. In: Melezhik, V.A., Prave, A.R., Fallick, A.E., Kump, L.R., Strauss, H., Lepland, A., Hanski, E.J.

- (Eds.). *Reading the Archive of Earth's Oxygenation*. In: *Frontiers in Earth Sciences*. Springer, Berlin Heidelberg, pp. 387–490.
- Miao, L., Moczyłowska, M., Zhu, S., Zhu, M., 2019. New record of organic-walled, morphologically distinct microfossils from the late Paleoproterozoic Changcheng Group in the Yanshan Range, North China. *Precambrian Res.* 321, 172–198. <https://doi.org/10.1016/j.precamres.2018.11.019>.
- Miletto, M., Wang, X., Planavsky, N.J., Luther, G.W., Lyons, T.W., Tebo, B.M., 2021. Marine microbial Mn(II) oxidation mediates Cr(III) oxidation and isotope fractionation. *Geochim. Cosmochim. Acta* 297, 101–119. <https://doi.org/10.1016/j.gca.2021.01.008>.
- Müller, M., Mentel, M., van Hellemond, J.J., Henze, K., Woehle, C., Gould, S.B., Yu, R.-Y., van der Geizen, M., Tielsens, A.G.M., Martin, W.F., 2012. Biochemistry and evolution of anaerobic energy metabolism in eukaryotes. *Microbiol. Mol. Biol. Rev.* 76, 444–495. <https://doi.org/10.1128/MMBR.05024-11>.
- Ossa Ossa, F., Eickmann, B., Hofmann, A., Planavsky, N.J., Asael, D., Pambo, F., Bekker, A., 2018. Two-step deoxygenation at the end of the Paleoproterozoic Lomagundi Event. *Earth Planet. Sci. Lett.* 486, 70–83. <https://doi.org/10.1016/j.epsl.2018.01.009>.
- Ovchinnikova, G.V., Kuznetsov, A.B., Melezhiuk, V.A., Gorokhov, I.M., Vasil'eva, I.M., Gorokhovskii, B.M., 2007. Pb-Pb age of Jatulian carbonate rocks: the Tulomozero Formation of southeast Karelia. *Stratigr. Geol. Correl.* 15, 359–372. <https://doi.org/10.1134/S0869593807040028>.
- Paiste, K., Lepland, A., Zerkle, A.L., Kirsimäe, K., Izon, G., Patel, N.K., McLean, F., Kreitsmann, T., Mänd, K., Bui, T.H., Romashkin, A.E., Rychanchik, D.V., Prave, A.R., 2018. Multiple sulphur isotope records tracking basinal and global processes in the 1.98 Ga Zaonega Formation, NW Russia. *Chem. Geol.* 499, 151–164. <https://doi.org/10.1016/j.chemgeo.2018.09.025>.
- Paiste, K., Lepland, A., Zerkle, A.L., Kirsimäe, K., Kreitsmann, T., Mänd, K., Romashkin, A.E., Rychanchik, D.V., Prave, A.R., 2020a. Identifying global vs. basinal controls on Paleoproterozoic organic carbon and sulfur isotope records. *Earth-Sci. Rev.* 207, 103230. <https://doi.org/10.1016/j.earscirev.2020.103230>.
- Paiste, K., Pellerin, A., Zerkle, A.L., Kirsimäe, K., Prave, A.R., Romashkin, A.E., Lepland, A., 2020b. The pyrite multiple sulfur isotope record of the 1.98 Ga Zaonega Formation: evidence for biogeochemical sulfur cycling in a semi-restricted basin. *Earth Planet. Sci. Lett.* 534, 116092. <https://doi.org/10.1016/j.epsl.2020.116092>.
- Parfrey, L.W., Lahr, D.J.G., Knoll, A.H., Katz, L.A., 2011. Estimating the timing of early eukaryotic diversification with multigene molecular clocks. *Proc. Natl. Acad. Sci. USA* 108, 13624–13629. <https://doi.org/10.1073/pnas.1110633108>.
- Partin, C.A., Bekker, A., Planavsky, N.J., Scott, C.T., Gill, B.C., Li, C., Podkovyrov, V., Maslov, A., Konhauser, K.O., Lalonde, S.V., Love, G.D., Poulton, S.W., Lyons, T.W., 2013. Large-scale fluctuations in Precambrian atmospheric and oceanic oxygen levels from the record of U in shales. *Earth Planet. Sci. Lett.* 369–370, 284–293. <https://doi.org/10.1016/j.epsl.2013.03.031>.
- Payne, J.L., Boyer, A.G., Brown, J.H., Finnegan, S., Kowalewski, M., Krause, R.A., Lyons, S.K., McClain, C.R., McShea, D.W., Novack-Gottshall, P.M., Smith, F.A., Stempien, J.A., Wang, S.C., 2009. Two-phase increase in the maximum size of life over 3.5 billion years reflects biological innovation and environmental opportunity. *Proc. Natl. Acad. Sci.* 106, 24–27. <https://doi.org/10.1073/pnas.0806314106>.
- Pérez-Fodich, A., Reich, M., Álvarez, F., Snyder, G.T., Schoenberg, R., Vargas, G., Muramatsu, Y., Fehn, U., 2014. Climate change and tectonic uplift triggered the formation of the Atacama Desert's giant nitrate deposits. *Geology* 42, 251–254. <https://doi.org/10.1130/G34969.1>.
- Planavsky, N.J., Bekker, A., Hofmann, A., Owens, J.D., Lyons, T.W., 2012. Sulfur record of rising and falling marine oxygen and sulfate levels during the Lomagundi event. *Proc. Natl. Acad. Sci. USA* 109, 18300–18305. <https://doi.org/10.1073/pnas.1120387109>.
- Planavsky, N.J., Reinhard, C.T., Wang, X., Thomson, D., McGoldrick, P., Rainbird, R.H., Johnson, T., Fischer, W.W., Lyons, T.W., 2014. Low Mid-Proterozoic atmospheric oxygen levels and the delayed rise of animals. *Science* 346, 635–638. <https://doi.org/10.1126/science.1258410>.
- Porter, S.M., 2020. Insights into eukaryogenesis from the fossil record. *Interface Focus* 10, 20190105. <https://doi.org/10.1098/rsfs.2019.0105>.
- Priyatikina, N., Khudoley, A.K., Ustinov, V.N., Kullerud, K., 2014. 1.92 Ga kimberlitic rocks from Kimozero, NW Russia: their geochemistry, tectonic setting and unusual field occurrence. *Precambrian Res.* 249, 162–179. <https://doi.org/10.1016/j.precamres.2014.05.009>.
- Puchtel, I.S., Arndt, N.T., Hofmann, A.W., Haase, K.M., Kröner, A., Kulikov, V.S., Kulikova, V.V., Garbe-Schönberg, C.-D., Nemchin, A.A., 1998. Petrology of mafic lavas within the Onega plateau, central Karelia: evidence for 2.0 Ga plume-related continental crustal growth in the Baltic Shield. *Contrib. Mineral. Petrol.* 130, 134–153. <https://doi.org/10.1007/s004100050355>.
- Puchtel, I.S., Brüggemann, G.E., Hofmann, A.W., 1999. Precise Re–Os mineral isochron and Pb–Nd–Os isotope systematics of a mafic–ultramafic sill in the 2.0 Ga Onega plateau (Baltic Shield). *Earth Planet. Sci. Lett.* 170, 447–461. [https://doi.org/10.1016/S0012-821X\(99\)00118-1](https://doi.org/10.1016/S0012-821X(99)00118-1).
- Qu, Y., Črne, A.E., Lepland, A., van Zuijlen, M.A., 2012. Methanotrophy in a Paleoproterozoic oil field ecosystem, Zaonega Formation, Karelia, Russia. *Geobiology* 10, 467–478. <https://doi.org/10.1111/gbi.12007>.
- Rasmussen, B., Bengtson, S., Fletcher, I.R., McNaughton, N.J., 2002. Discoidal impressions and trace-like fossils more than 1200 million years old. *Science* 296, 1112–1115. <https://doi.org/10.1126/science.1070166>.
- Reinhard, C.T., Planavsky, N.J., Robbins, L.J., Partin, C.A., Gill, B.C., Lalonde, S.V., Bekker, A., Konhauser, K.O., Lyons, T.W., 2013. Proterozoic ocean redox and biogeochemical stasis. *Proc. Natl. Acad. Sci. USA* 110, 5357–5362. <https://doi.org/10.1073/pnas.1208622110>.
- Reinhard, C.T., Planavsky, N.J., Wang, X., Fischer, W.W., Johnson, T.M., Lyons, T.W., 2014. The isotopic composition of authigenic chromium in anoxic marine sediments: a case study from the Cariaco Basin. *Earth Planet. Sci. Lett.* 407, 9–18. <https://doi.org/10.1016/j.epsl.2014.09.024>.
- Reinhard, C.T., Planavsky, N.J., Ward, B.A., Love, G.D., Hir, G.L., Ridgwell, A., 2020. The impact of marine nutrient abundance on early eukaryotic ecosystems. *Geobiology* 18, 139–151. <https://doi.org/10.1111/gbi.12384>.
- Robbins, L.J., Lalonde, S.V., Planavsky, N.J., Partin, C.A., Reinhard, C.T., Kendall, B., Scott, C., Hardisty, D.S., Gill, B.C., Alessi, D.S., Dupont, C.L., Saito, M.A., Crowe, S.A., Poulton, S.W., Bekker, A., Lyons, T.W., Konhauser, K.O., 2016. Trace elements at the intersection of marine biological and geochemical evolution. *Earth-Sci. Rev.* 163, 323–348. <https://doi.org/10.1016/j.earscirev.2016.10.013>.
- Rodler, A., Sánchez-Pastor, N., Fernández-Díaz, L., Frei, R., 2015. Fractionation behavior of chromium isotopes during coprecipitation with calcium carbonate: implications for their use as paleoclimatic proxy. *Geochim. Cosmochim. Acta* 164, 221–235. <https://doi.org/10.1016/j.gca.2015.05.021>.
- Rosenbaum, J., Sheppard, S.M.F., 1986. An isotopic study of siderites, dolomites and ankerites at high temperatures. *Geochim. Cosmochim. Acta* 50, 1147–1150. [https://doi.org/10.1016/0016-7037\(86\)90396-0](https://doi.org/10.1016/0016-7037(86)90396-0).
- Saad, E.M., Wang, X., Planavsky, N.J., Reinhard, C.T., Tang, Y., 2017. Redox-independent chromium isotope fractionation induced by ligand-promoted dissolution. *Nat. Commun.* 8, 1–10. <https://doi.org/10.1038/s41467-017-01694-y>.
- Schoenberg, R., Zink, S., Staubwasser, M., von Blanckenburg, F., 2008. The stable Cr isotope inventory of solid Earth reservoirs determined by double spike MC-ICP-MS. *Chem. Geol.* 249, 294–306. <https://doi.org/10.1016/j.chemgeo.2008.01.009>.
- Shih, P.M., Matzke, N.J., 2013. Primary endosymbiosis events date to the later Proterozoic with cross-calibrated phylogenetic dating of duplicated ATPase proteins. *Proc. Natl. Acad. Sci.* 110, 12355–12360. <https://doi.org/10.1073/pnas.1305813110>.
- Sperling, E.A., Stockey, R.G., 2018. The temporal and environmental context of early animal evolution: considering all the ingredients of an “Explosion”. *Integr. Comp. Biol.* 58, 605–622. <https://doi.org/10.1093/icb/icy088>.
- Sperling, E.A., Frieder, C.A., Raman, A.V., Girguis, P.R., Levin, L.A., Knoll, A.H., 2013. Oxygen, ecology, and the Cambrian radiation of animals. *Proc. Natl. Acad. Sci.* 110, 13446–13451. <https://doi.org/10.1073/pnas.1312778110>.
- Stepanova, A., Samsonov, A., Larionov, A., 2014. The final episode of middle Proterozoic magmatism in the Onega structure: data on trans-Onega dolerites. *Trans. Karelian Res. Cent. Russ. Acad. Sci. Precambrian Geol. Ser.* 1, 3–16.
- Tang, D., Shi, X., Ma, J., Jiang, G., Zhou, X., Shi, Q., 2017. Formation of shallow-water glaucony in weakly oxygenated Precambrian ocean: an example from the Mesoproterozoic Tieling Formation in North China. *Precambrian Res.* 294, 214–229. <https://doi.org/10.1016/j.precamres.2017.03.026>.
- Toma, J., Holmden, C., Shakotko, P., Pan, Y., Ootes, L., 2019. Cr isotopic insights into ca. 1.9 Ga oxidative weathering of the continents using the Beaverledge Lake paleosol, Northwest Territories, Canada. *Geobiology* 17, 467–489. <https://doi.org/10.1111/gbi.12342>.
- Turner, E.C., 2021. Possible poriferan body fossils in early Neoproterozoic microbial reefs. *Nature* 596, 87–91. <https://doi.org/10.1038/s41586-021-03773-z>.
- Waldbauer, J.R., Newman, D.K., Summons, R.E., 2011. Microaerobic steroid biosynthesis and the molecular fossil record of Archean life. *Proc. Natl. Acad. Sci.* 108, 13409–13414. <https://doi.org/10.1073/pnas.1104160108>.
- Ward, P., Labandeira, C., Laurin, M., Berner, R.A., 2006. Confirmation of Romer's Gap as a low oxygen interval constraining the timing of initial arthropod and vertebrate terrestrialization. *Proc. Natl. Acad. Sci.* 103, 16818–16822. <https://doi.org/10.1073/pnas.0607824103>.
- Warke, M.R., Rocco, T.D., Zerkle, A.L., Lepland, A., Prave, A.R., Martin, A.P., Ueno, Y., Condon, D.J., Claire, M.W., 2020. The Great Oxidation Event preceded a Paleoproterozoic “snowball Earth”. *Proc. Natl. Acad. Sci.* 117, 13314–13320. <https://doi.org/10.1073/pnas.2003090117>.
- Wei, W., Frei, R., Kläbe, R., Tang, D., Wei, G.-Y., Li, D., Tian, L.-L., Huang, F., Ling, H.-F., 2021. A transient swing to higher oxygen levels in the atmosphere and oceans at ~1.4 Ga. *Precambrian Res.* 354, 106058. <https://doi.org/10.1016/j.precamres.2020.106058>.
- Wei, W., Kläbe, R., Ling, H.-F., Huang, F., Frei, R., 2020. Biogeochemical cycle of chromium isotopes at the modern Earth's surface and its applications as a paleo-environment proxy. *Chem. Geol.* 541, 119570. <https://doi.org/10.1016/j.chemgeo.2020.119570>.
- Xiao, S., Laflamme, M., 2009. On the eve of animal radiation: phylogeny, ecology and evolution of the Ediacara biota. *Trends Ecol. Evol.* 24, 31–40. <https://doi.org/10.1016/j.tree.2008.07.015>.
- Zhang, K., Zhu, X., Wood, R.A., Shi, Y., Gao, Z., Poulton, S.W., 2018. Oxygenation of the Mesoproterozoic ocean and the evolution of complex eukaryotes. *Nat. Geosci.* 11, 345–350. <https://doi.org/10.1038/s41561-018-0111-y>.